

000 001 002 003 004 005 GLSTM: MITIGATING OVER-SQUASHING BY 006 INCREASING STORAGE CAPACITY 007 008 009

010 **Anonymous authors**
011 Paper under double-blind review
012
013
014
015
016
017
018
019
020
021
022
023
024

ABSTRACT

025 Graph Neural Networks (GNNs) leverage the graph structure to transmit information
026 between nodes, typically through the message-passing mechanism. While
027 these models have found a wide variety of applications, they are known to suffer from *over-squashing*, where information from a large receptive field of node
028 representations is collapsed into a single fixed sized vector, resulting in an information
029 bottleneck. In this paper, we re-examine the over-squashing phenomenon
030 through the lens of model *storage and retrieval capacity*, which we define as the
031 amount of information that can be stored in a node’s representation for later use.
032 We study some of the limitations of existing tasks used to measure over-squashing
033 and introduce a new synthetic task to demonstrate that an information bottleneck
034 can saturate this capacity. Furthermore, we adapt ideas from the sequence modeling
035 literature on associative memories, fast weight programmers, and the xLSTM
036 model to develop a novel GNN architecture with improved capacity. We demonstrate
037 strong performance of this architecture both on our capacity synthetic task,
038 as well as a range of real-world graph benchmarks.
039

1 INTRODUCTION

040 Graph Neural Networks (GNNs) (Sperduti, 1993; Gori et al., 2005; Scarselli et al., 2008; Micheli,
041 2009; Bruna et al., 2014; Defferrard et al., 2017) have emerged as a standard framework for learning
042 on graph-structured data. The majority of these models follow a *message passing* paradigm, where
043 nodes iteratively exchange information with neighbors, commonly referred to as Message-Passing
044 Neural Networks (MPNNs). Examples of this family of architectures include GCN (Kipf & Welling,
045 2017), GAT (Veličković et al., 2018), GIN (Xu et al., 2018), and GraphSAGE (Hamilton et al., 2017).
046

047 Since each MPNN layer exchanges information between neighboring nodes to update node representations,
048 the number of layers thus dictates the receptive field: the set of nodes over which information is aggregated.
049 Deep MPNNs are, in theory, desirable as they can model long-range dependencies, but scaling to many layers has historically been difficult due to two pervasive issues that have received significant attention in the literature: *over-smoothing* and *over-squashing*. We focus on the latter in this work.
050

051 Over-squashing was initially identified by Alon & Yahav (2021) as a problem of compressing information from a node’s receptive field into a fixed-size vector. This was linked with depth and long-range dependencies, since receptive fields tend to grow exponentially with depth. Later work (Topping et al., 2022; Di Giovanni et al., 2023a) identified that this bottleneck could also result in low sensitivity as measured by the node Jacobian, linking graph topology and aspects of model architecture via an upper bound on this Jacobian. This low sensitivity arises due to repeated degree normalization and application of a contractive nonlinearity over many layers. Arnaiz-Rodriguez & Errica (2025) suggest that these two descriptions of over-squashing are not the same, and that Alon & Yahav (2021) define it as a problem of computational graph bottlenecks, while later work often defines it as a problem of topological bottlenecks. We discuss this separation and its relation to our work in Appendix A.
052

053 Instead of separating by issues of computational tree structure and bottlenecks, we suggest an alternative separation by resultant *failure mode*: limited information storage capacity, and low sensitivity. In light of this, we highlight another divergence in the literature: the work of Alon & Yahav (2021) implicitly described over-squashing as a capacity problem, and later work re-framed it as a problem
054

of sensitivity. Focusing on the failure modes themselves not only allows us to revisit the issue of capacity originally discussed in Alon & Yahav (2021), but also to more directly motivate benchmarks and remedies, both of which we discuss in this paper. We further contextualize this issue of capacity by studying it in *isolation* from sensitivity issues. We believe this focus not only provides a more complete understanding of over-squashing but also highlights new directions to mitigate it.

To combat over-squashing, existing research has focused on ameliorating topological bottlenecks through *rewiring* (Gasteiger et al., 2019; Gutteridge et al., 2023; Nguyen et al., 2023) and controlling the flow of information (Bresson & Laurent, 2017; Finkelshtein et al., 2024; Errica et al., 2025) – targeting topological and general computational bottlenecks respectively. However, these bottlenecks are only an issue if they harm performance in some way: in this work we discuss issues of (1) reduced sensitivity and (2) saturated storage capacity. Our proposed architecture in Section 4 targets the latter failure mode: adapting the MPNN architecture to improve its *ability to store and retrieve information*. Framing over-squashing as a capacity limitation that can be addressed at the architecture level exposes a previously unexplored path, and our results validate this direction.

To improve MPNN storage capacity we turn to the sequence modeling literature, which has a long history of tackling equivalent problems (Hochreiter & Schmidhuber, 1997; Orvieto et al., 2023; Gu & Dao, 2023; Beck et al., 2024; Arora et al., 2024). Taking inspiration from these works, we introduce an MPNN architecture that utilizes associative memory (Beck et al., 2024; Schlag et al., 2021; Hopfield, 1982), and demonstrate that this exhibits improved storage capacity.

Contributions. Our main contributions are as follows. In Section 3, we **re-characterize over-squashing into two distinct failure modes**: *saturating capacity* and *low sensitivity*, which we term capacity over-squashing and sensitivity over-squashing respectively. We discuss in Section 3.1 the pitfalls of widely used over-squashing tasks, which either fail to evaluate capacity at all, or evaluate the two issues in tandem and are thus unable to separate their effects. In Section 3.2, we introduce a novel synthetic task, which to our knowledge is the first that **measures capacity over-squashing in isolation**. In Section 4, we present a new MPNN architecture based on the recent xLSTM architecture (Beck et al., 2024), which uses **associative memory to increase capacity**, explicitly targeting this capacity over-squashing viewpoint. Section 5 demonstrates that this architecture performs well on our synthetic capacity task and a range of real-world benchmarks, and Section 5.2 demonstrates empirically that **capacity over-squashing can occur separately from sensitivity over-squashing**.

2 BACKGROUND AND RELATED WORK

Message Passing Neural Networks Let a graph \mathcal{G} be a tuple $(\mathcal{V}, \mathcal{E})$ where \mathcal{V} is the set of nodes and \mathcal{E} the set of edges. An edge from node u to v is denoted $(u, v) \in \mathcal{E}$. The connectivity is encoded by the adjacency matrix $\mathbf{A} \in \mathbb{R}^{|\mathcal{V}| \times |\mathcal{V}|}$, where $\mathbf{A}_{uv} = 1$ if $(u, v) \in \mathcal{E}$ and 0 otherwise. Each node v has a feature vector $\mathbf{x}_v \in \mathbb{R}^d$.

GNNs are functions $f_{\theta} : (\mathcal{G}, \{\mathbf{x}_v\}) \mapsto \mathbf{y}$ with parameters θ , trained via gradient descent to predict node- or graph-level labels \mathbf{y} . These models typically take the form of MPNNs, which compute latent representations by composing L layers of the following node-wise operation:

$$\mathbf{h}_u^{(l)} = \phi^{(l)}(\mathbf{h}_u^{(l-1)}, \psi^{(l)}(\{\mathbf{h}_v^{(l-1)} : (u, v) \in \mathcal{E}\})), \quad (1)$$

where $\psi^{(l)}$ is a permutation-invariant *aggregator*, $\phi^{(l)}$ combines neighbor messages with the previous embedding and $\mathbf{h}_v^{(0)} = \mathbf{x}_v$. Throughout, we use “GNN” and “MPNN” interchangeably. Note we depart from the more usual notation of k for layer index to avoid confusion with *keys*, introduced in Section 3.2. The most commonly used aggregation function takes the form

$$\psi^{(l)}(\{\mathbf{h}_v^{(l-1)} : (u, v) \in \mathcal{E}\}) = \sum_v \mathbf{O}_{uv} \mathbf{h}_v^{(l-1)}, \quad (2)$$

where $\mathbf{O} \in \mathbb{R}^{|\mathcal{V}| \times |\mathcal{V}|}$ is some message-passing matrix. For GCN (Kipf & Welling, 2017), $\mathbf{O} = \tilde{\mathbf{D}}^{-1/2} \tilde{\mathbf{A}} \tilde{\mathbf{D}}^{-1/2}$ with $\tilde{\mathbf{A}} = \mathbf{A} + \mathbf{I}$ for diagonal $\tilde{\mathbf{D}} \in \mathbb{R}^{|\mathcal{V}| \times |\mathcal{V}|}$ with $\tilde{\mathbf{D}}_{ii} = \sum_j \tilde{\mathbf{A}}_{ij}$. We frequently denote the set of message-passing neighbors of node u as $\mathcal{N}_u = \{v \in \mathcal{V} \mid \mathbf{O}_{uv} \neq 0\}$ – if the message-passing matrix is layer-dependent, we may superscript this with a layer index.

108 **Fast Weight Programmers** Fast Weight Programmers (FWPs) are a class of neural network motivated
 109 by the idea of allowing variable network weights dependent on the input - termed *fast weights*.
 110 One method to “program” the fast weights is to take outer products of learned projections of the
 111 input (Schmidhuber, 1992). Schlag et al. (2021) observe that – up to normalization and activation
 112 function differences – linear Transformers (Katharopoulos et al., 2020) are equivalent to FWPs.

113 **xLSTM: Associative Memory for Language Modeling** Recent work Beck et al. (2024; 2025)
 114 introduced xLSTM, a development of the original LSTM Hochreiter & Schmidhuber (1997) architecture
 115 that resulted in a performant recurrent neural network capable of language modeling. Of
 116 relevance to our work are the following limitations that xLSTM aims to address: the inability to
 117 “revise storage decisions” and the limited storage capacity of the scalar cell states. The first of these
 118 is addressed through modifying the original LSTM gating to use exponential activation functions.
 119 The second is addressed by introducing associative memory, updated using an outer product update
 120 rule equivalent to that of FWPs to store keys and values (see Appendix B for more details).

122 3 THE TWO FAILURE MODES OF OVER-SQUASHING

124 Over-squashing was initially introduced by Alon & Yahav (2021) as an issue of **storage capacity**.
 125 They observed that recurrent sequence models exhibit a bottleneck in representing all the information
 126 from their past inputs, and this bottleneck exists in a more harmful form in GNNs, in which
 127 the information receptive field grows exponentially. They introduced a synthetic task to measure
 128 over-squashing by propagating information through various sizes of binary tree.

129 Later research identified that this computational graph bottleneck *also* resulted in **low sensitivity** and
 130 issues of signal propagation. Topping et al. (2022); Di Giovanni et al. (2023a) quantified this low
 131 sensitivity via the Jacobian of node representations, establishing the following sensitivity bound: for
 132 an MPNN with l layers, c_σ Lipschitz constant of the activation, w maximal entry-value over weight
 133 matrices, d embedding dimension and $u, v \in \mathcal{V}$, one has

$$135 \quad \left\| \frac{\partial \mathbf{h}_v^{(l)}}{\partial \mathbf{h}_u^{(0)}} \right\|_{L_1} \leq \underbrace{(c_\sigma w d)^l}_{\text{model}} \underbrace{(\mathbf{O}^l)_{uv}}_{\text{topology}}, \quad (3)$$

138 where \mathbf{O} is the message passing matrix used by the MPNN as in Equation (2). This bound estab-
 139 lishes that low sensitivity results from both graph topology as well as factors intrinsic to the MPNN
 140 model. In particular, sensitivity is lowered by the nature of the message-passing, where the culprit
 141 is successive powers of a degree-normalized adjacency matrix. It is also lowered by the contractive
 142 nature of the nonlinearity σ and the values of the weight matrices, as established in (Arroyo et al.,
 143 2025). Despite this analysis being purely one of sensitivity rather than capacity, it was also termed
 144 over-squashing, and has been successful in establishing links to other areas, including the expressive
 145 power of MPNNs (Di Giovanni et al., 2023b) and graph effective resistance (Black et al., 2023).

146 We argue that there are two *distinct* problems arising from bottlenecks in MPNNs: *reduced sensi-
 147 tivity* (sensitivity over-squashing) and *saturating storage capacity* (capacity over-squashing). Due
 148 to the influential paper of Topping et al. (2022) the sensitivity viewpoint on over-squashing has thus
 149 been the predominant approach in the literature; **in this work, we seek to revisit the storage
 150 capacity viewpoint** and investigate how this issue can be avoided. We define storage capacity as the
 151 amount of information that can be stored in a node’s representation for later use: a representation is
 152 *saturated* when it is unable to store any more information.

153 **Conflation With Depth** The vast majority of existing research links over-squashing with depth.
 154 To an extent, this is justified: the bound of Equation (3) decreases exponentially with MPNN depth,
 155 and real-world graphs tend to exhibit receptive fields that grow exponentially in depth, leading to
 156 capacity quickly becoming a problem for deep MPNNs. However, alongside recent work (Arnaiz-
 157 Rodriguez & Errica, 2025), we highlight that over-squashing is not *exclusively* a problem of depth:
 158 bottlenecks can be observed in single-layer GNNs acting on high-degree nodes – we exploit this
 159 fact in our synthetic task of Section 3.2. Furthermore, in studying over-squashing only in the
 160 *deep regime*, much of the literature has conflated the problem with issues of *vanishing gradients*,
 161 themselves closely linked to the related problem of *over-smoothing* Di Giovanni et al. (2023b).
 Arroyo et al. (2025) give a more precise treatment of how the issue of over-squashing relates to

162 depth, through over-smoothing (zero collapse) and vanishing gradients. In this work we study over-
 163 squashing in the *shallow regime*: this allows us to isolate the issue of saturating capacity, avoiding
 164 the effects of depth on both reduced sensitivity (Equation (3)) and vanishing gradients.
 165

166 3.1 EXISTING OVER-SQUASHING TASKS DO NOT (ONLY) TEST CAPACITY

167 An instructive way of contrasting sensitivity against
 168 capacity is via synthetic tasks. The most common
 169 of these used to assess over-squashing are the Ring-
 170 Transfer tasks of Di Giovanni et al. (2023a). The
 171 goal of these tests is for a MPNN to ‘transfer’ fea-
 172 tures contained at a target node to a source node,
 173 across a large graph distance. Various graphs are
 174 tested, in particular a ring of nodes, but the common
 175 feature is that there exists a long shortest-path from
 176 the source to target node. All of these exhibit an
 177 exponentially growing receptive field of at least 2^k
 178 for k layers, since each node is connected to at least
 179 two others; repeated aggregation and application of
 180 MPNN layers and nonlinearities makes this a good
 181 test of the sensitivity-based view of over-squashing.
 182

183 However, this task is particularly ill-equipped to
 184 test the issue of storage capacity, as the *only* re-
 185 relevant information in the graph is that of the target
 186 node, and all intermediate nodes are assigned con-
 187 stant vectors of ones. In this way, there is only a sin-
 188 gle node’s representation worth of information to be
 189 transferred. It is unclear how much this task mea-
 190 sures behavior found in real-world tasks: expon-
 191 entially growing receptive fields will not be padded by
 192 nodes with identical representations. Figure 1 (left)
 193 visualizes the computational graph of RingTransfer,
 194 demonstrating that it is dominated by nodes con-
 195 taining no information. Therefore, this task exhibits
 196 a large computational bottleneck without any issues
 197 of saturating capacity: this highlights the fact that,
 198 beyond the computational bottleneck, saturated ca-
 199 pacity is at least also dependent on the information
 200 content of the task.

201 Alon & Yahav (2021) introduced the Tree-NeighborsMatch task to measure capacity by prop-
 202 agating information from the leaf nodes of a variable-size binary tree. It shares similarities with
 203 the task we introduce in Section 3.2 in that it controls the amount of information that is forced into
 204 a single node representation. However, it propagates this information through a deep binary tree,
 205 requiring variable-depth MPNNs. This significantly harms sensitivity: we visualize Jacobian norms
 206 of a GCN acting on a deep binary tree vs a single layer tree with matching leaf counts in Figure 2,
 207 demonstrating that this sensitivity drops off far faster for deep GCNs. This is unsurprising given
 208 the bound of Equation (3): deep GCNs must additionally contend with “model” squashing terms
 209 of nonlinearity and weight contraction that scale exponentially with depth. Therefore performance
 210 degradation trends are due to both 1) saturating capacity and 2) low sensitivity; deep tasks such as
 211 Tree-NeighborsMatch are impacted by both over-squashing issues, rather than isolating the
 212 issue of capacity.

213 3.2 NEIGHBOR ASSOCIATIVE RECALL: ISOLATING STORAGE CAPACITY

214 We investigate storage capacity by measuring *associative recall*: this is a common approach taken
 215 in the sequence-modeling literature (Ba et al., 2016; Schlag et al., 2021; Arora et al., 2024; Jelassi
 et al., 2024), in which the question of model storage capacity is also clearly of interest. These

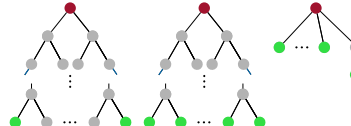


Figure 1: Computational graphs. **Left:** Ring-Transfer (Di Giovanni et al., 2023a). **Middle:** Tree-NeighborsMatch (Alon & Yahav, 2021). **Right:** NAR, introduced in Section 3.2. Nodes with informative features are green, background gray. Red node is trained to solve the task.

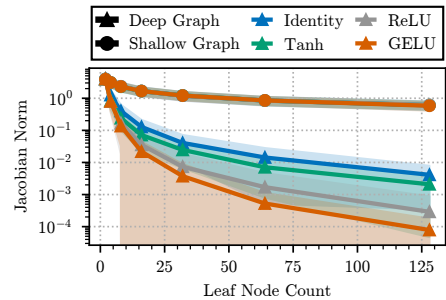


Figure 2: Log Jacobian norms. “Deep” graphs are binary trees of Tree-NeighborsMatch (Alon & Yahav, 2021); “Shallow” graphs are single-level trees with the same number of leaves. A GCN of depth equal to the tree depth acts on each. Jacobian norms are $|\partial \mathbf{h}_r^{(L)} / \partial \mathbf{h}_l^{(0)}|_1$ for root r and leaf l (red/green in Figure 1). Shaded area is standard deviation.

216 synthetic tasks involve presenting the model with a sequence of key value pairs followed by a query
 217 that corresponds to one of the presented keys, and the model must return the associated value.
 218

219 To this end, we introduce a task that we refer to as Neighbor Associative Recall (NAR). Whereas
 220 the sequence associative recall tasks measure the ability of a model to recall previous information
 221 from a variable-length sequence, our graph adaptation is designed to measure the ability of a GNN
 222 to recall information from the previous message passing round over a variable number of neighbors.
 223

224 The task is designed as follows. For a given neighborhood size N we create a graph of $N + 3$ nodes.
 225 This graph consists of N “neighbor” nodes, a central node to which they are all connected, an inter-
 226 mediate node connected to the central node, and a “query” node connected only to the intermediate
 227 node. An example such graph is visualized in Figure 3.

228 For a fixed neighborhood size N we define a fixed set
 229 of keys and values, $N = |\mathbb{K}| = |\mathbb{V}|$, and a pair of
 230 learned vector embedding functions $e_k : \mathbb{K} \rightarrow \mathbb{R}^{d_{emb}}$,
 231 $e_v : \mathbb{V} \rightarrow \mathbb{R}^{d_{emb}}$ for embedding dimension d_{emb} . Each
 232 of the neighbor nodes n has a different assigned key
 233 $k_n \in \mathbb{K}$, and also a value $v_n \in \mathbb{V}$, randomly sam-
 234 pled with replacement. The input feature vector of these
 235 nodes is a concatenation of the two learned embeddings
 236 $x_n = [e_k(k_n); e_v(v_n)] \in \mathbb{R}^{2d_{emb}}$. The intermediate node
 237 and central node both have zero-valued feature vectors.
 238 Associated with the query node q is a randomly sampled
 239 key-value node m ; the input feature vector for the query
 240 node consists of the corresponding key embedding con-
 241 catenated with a vector of zeroes, $x_q = [e_k(k_m); \mathbf{0}] \in$
 242 $\mathbb{R}^{2d_{emb}}$. The model is trained such that the central node
 243 must predict the value v_m associated with the sampled
 244 key node. Training is via cross-entropy loss where the tar-
 245 get of the central node is a one-hot vector corresponding
 246 to a fixed ordering of \mathbb{V} . This approach can be viewed as a
 247 graph adaptation of the sequence associative recall task of
 248 Schlag et al. (2021). Results are presented in Section 5.1.
 249 An alternative formulation of this task with a regression target is discussed in Appendix D.8.
 250

251 NAR is designed such that the receptive field of the central node will comprise *only* the neighbor
 252 nodes in the first layer. In order to perfectly solve the task, it must store all of the key-value informa-
 253 tion in this initial receptive field, as it is impossible to limit the scope of the information that might
 254 later be required. In the second layer, the receptive field will include the query node: now, the model
 255 must selectively recall the correct value from its immediate neighbors.
 256

257 This task is novel as it assesses over-squashing in the shallow regime: MPNNs tested in Section 5.1
 258 consist of just two message passing layers. This more effectively isolates the issue of capacity,
 259 without secondary effects from low sensitivity and vanishing gradients as visualized in Figure 2.
 260

4 GLSTM: COMBINING GRAPH NETWORKS AND ASSOCIATIVE MEMORY

261 Prior work on over-squashing has focused almost exclusively on mitigating sensitivity issues, often
 262 through graph rewiring (Gasteiger et al., 2019; Gutteridge et al., 2023; Nguyen et al., 2023). Some
 263 work has implicitly tackled capacity over-squashing by moderating the flow of information into node
 264 representations (Bresson & Laurent, 2017; Finkelshtein et al., 2024; Errica et al., 2025) thus reducing
 265 capacity requirements, but we are unaware of any work that has attempted to *increase* capacity at an
 266 architecture level. Motivated by memory-capacity gains in sequence models (Ba et al., 2016; Beck
 267 et al., 2024), we introduce associative memory into an MPNN architecture to explicitly enlarge its
 268 information-storage capacity; we measure this in the graph setting using the NAR task introduced
 269 above. We further introduce the gating scheme of Beck et al. (2024) to investigate its efficacy in the
 270 graph setting, given strong sequence modeling performance. Since these adaptations are inspired in
 271 part by their successful use in xLSTM, we refer to our related graph architecture as gLSTM.
 272

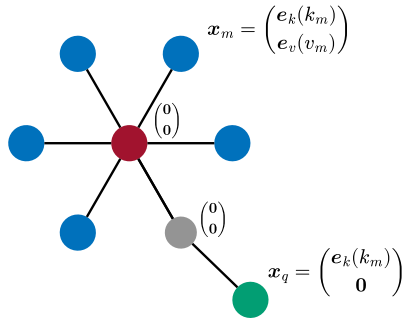


Figure 3: An example graph with $N = 5$ from the NAR task. Key-value nodes are shown in blue, the central node in red and the query node in green. In this graph, m is the randomly sampled index of the key-value node associated with query node q . The target for this graph is a one-hot vector corresponding to v_m .

For any node u at layer l , in addition to the usual MPNN vector hidden state $\mathbf{h}_u^{(l)}$, gLSTM maintains a matrix hidden state $\mathbf{C}_u^{(l)}$. The initial hidden state $\mathbf{h}_u^{(0)}$ is the input node feature vector \mathbf{x}_u . Keys and values are used to update $\mathbf{C}_u^{(l)}$ via an FWP-style outer product rule: these are projections of the previous vector hidden state $\mathbf{h}_u^{(l-1)}$. The next vector hidden state $\mathbf{h}_u^{(l)}$ is determined by “querying” $\mathbf{C}_u^{(l)}$ via matrix multiplication with another projection of the previous vector hidden states.

The modified gLSTM update equations are given below. Highlighted in blue are the differences to xLSTM. Biases correspond exactly to xLSTM (Appendix B) and are omitted for clarity.

State (and normalization) updates:

$$\mathbf{C}_u^{(l)} = f_u^{(l)} \mathbf{C}_u^{(l-1)} + \sum_{v \in \mathcal{N}_u^{(l)} \cup \{u\}} i_v^{(l)} \mathbf{v}_v^{(l)} \otimes \mathbf{k}_v^{(l)}$$

$$\mathbf{n}_u^{(l)} = f_u^{(l)} \mathbf{n}_u^{(l-1)} + \sum_{v \in \mathcal{N}_u^{(l)} \cup \{u\}} i_v^{(l)} \mathbf{k}_v^{(l)}$$

$$m_u^{(l)} = \max \left(\left\{ \tilde{f}_u^{(l)} + m_u^{(l-1)} \right\} \cup \left\{ \tilde{i}_v^{(l)} \mid \forall v \in \mathcal{N}_u^{(l)} \cup \{u\} \right\} \right)$$

Query / Key / Value computation:

$$\mathbf{q}_u^{(l)} = \mathbf{W}_q \left[\mathbf{h}_u^{(l-1)}; \sum_{v \in \mathcal{N}_u^{(l)}} \mathbf{h}_v^{(l-1)} \right]$$

$$\mathbf{k}_u^{(l)} = \frac{1}{\sqrt{d}} \mathbf{W}_k \mathbf{h}_u^{(l-1)}$$

$$\mathbf{v}_u^{(l)} = \mathbf{W}_v \mathbf{h}_u^{(l-1)}$$

The square brackets above denote vector concatenation. Concatenating the hidden state for the node and its neighbours in this way keeps them separate and allows the query – which will determine what is retrieved from the matrix memory – to *separately* depend on both the previous state of the node itself and the previous states of its neighbours.

Gate computation:

$$i_u^{(l)} = \exp \left(\tilde{i}_u^{(l)} - m_u^{(l)} \right) \quad \tilde{i}_u^{(l)} = \mathbf{w}_i^T \mathbf{h}_u^{(l-1)}$$

$$f_u^{(l)} = \exp \left(\tilde{f}_u^{(l)} + m_u^{(l-1)} - m_u^{(l)} \right) \quad \tilde{f}_u^{(l)} = \mathbf{w}_f^T \mathbf{h}_u^{(l-1)}$$

$$o_u^{(l)} = \sigma \left(\tilde{o}_u^{(l)} \right) \quad \tilde{o}_u^{(l)} = \mathbf{W}_o \mathbf{h}_u^{(l-1)}$$

Output:

$$\tilde{\mathbf{h}}_u^{(l)} = \frac{\mathbf{C}_u^{(l)} \mathbf{q}_u^{(l)}}{\max \left\{ \left| \mathbf{n}_u^{(l)} \top \mathbf{q}_u^{(l)} \right|, 1 \right\}}$$

$$\mathbf{h}_u^{(l)} = \mathbf{o}_u^{(l)} \odot \tilde{\mathbf{h}}_u^{(l)}$$

Block Structure Arroyo et al. (2025) note that sensitivity over-squashing issues are largely caused by vanishing gradients – a phenomenon well-explored in the sequence-modeling literature. In an attempt to address this, gLSTM therefore uses a similar block structure to the mLSTM block upon which it is based. Of particular importance is the residual connection – which brings the norm of the layer-wise Jacobian to the edge of chaos – and use of input and hidden norms, which regulate the magnitude of the Jacobian norms. Figure 4 visualizes the block structure of gLSTM that we employ.

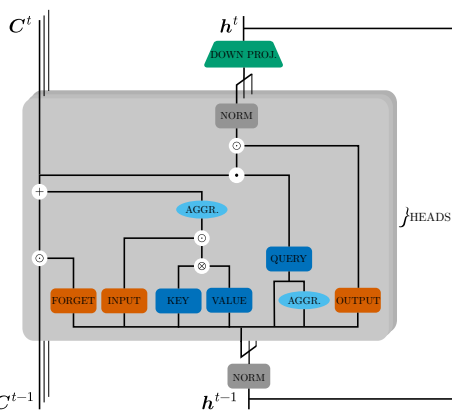


Figure 4: gLSTM block structure. Gates shown in orange, query/key/value in dark blue. Aggr. represents aggregation across neighborhoods. Symbols $\odot, \otimes, +, \cdot$ denote Hadamard product, outer product, vector addition, matrix multiplication.

K-Hop Aggregation Following Arroyo et al. (2025) we combine the memory capabilities of the xLSTM block with a *highly connected* message passing graph structure: employing a k-hop aggregation scheme. In this setting, each node u at layer l will aggregate information from the neighborhood

$$\mathcal{N}_u^{(l)} = \{v \in \mathcal{V} \mid d_{\mathcal{G}}(u, v) = l\},$$

where $d_{\mathcal{G}} : \mathcal{V} \times \mathcal{V} \rightarrow \mathbb{R}_{\geq 0}$ is the length of the minimal walk connecting nodes u and v . This approach resembles that of Ding et al. (2024), but with an additional recurrence: hidden states are used as input at each step. This substantially changes the way information can propagate through the graph. Furthermore, it also has links to ChebNet (Defferrard et al., 2017), which has recently been found to perform strongly on long-range tasks (Hariri et al., 2025).

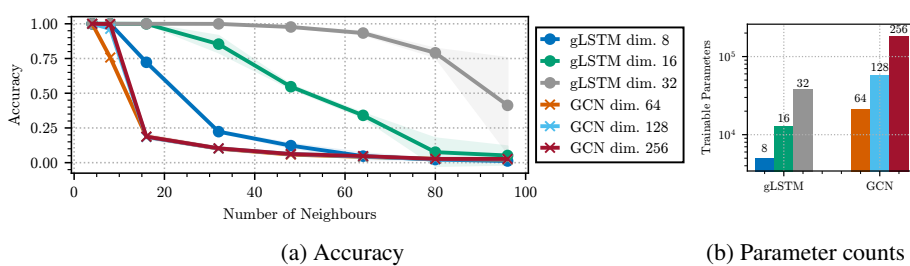
324 This aggregation scheme appears to greatly improve gLSTM performance: our synthetic task in Section 5.1 significantly benefits from this aggregation scheme, and the ablations in Appendix D.2 demonstrate that it improves performance in all 325 but one of the tested benchmarks. We hypothesize that – in addition to providing a highly connected 326 computational graph that lessens over-squashing sensitivity bottleneck issues – this is because it also 327 provides an extremely useful inductive bias for the *recall* mechanism of gLSTM. Information that 328 has previously been stored in the associative memory is not then included in later message passing 329 rounds, and later nodes are able to query this memory in isolation.

332 5 EXPERIMENTS

333 5.1 NEIGHBOR ASSOCIATIVE RECALL

334 We train various models on NAR with varying neighbor count N , with results shown in Figure 5a. 335 Throughout this section we compare gLSTM using K-hop aggregation to GCN using standard 336 aggregation, since gLSTM performs significantly better in this task when using K-hop aggregation 337 whereas GCN performance is harmed by K-hop. We present additional results in Appendix D.7 338 where we separate by aggregation method and include results for a larger number of models. A 339 comparison of the number of trainable parameters is shown in Figure 5b. Fair comparison between 340 matrix and vector memory is nontrivial, so we select these parameter counts to “favor” GCN.

341 These results demonstrate that gLSTM shows significantly improved recall abilities compared to 342 GCN. gLSTM retains perfect recall until the number of neighbors equals the memory dimension of 343 the model: beyond this is where capacity over-squashing appears to become a problem. This agrees 344 with intuition, since the maximum number of orthogonal key vectors (and separately, value vectors) 345 is equal to the memory dimension. However, it is interesting to note how the performance decreases 346 slowly as the neighbor count exceeds this limit, particularly for higher memory dimensions: this 347 appears to be a graph analog of the “graceful saturation” described by Smolensky (1990). By contrast, 348 capacity over-squashing starts much earlier at just $N = 8$ for the largest GCN model tested.



357 Figure 5: Test-set mean Accuracy (standard deviation shaded) for the NAR task, for gLSTM and 358 GCN models with various hidden dimensions shown in Figure 5a, number of trainable parameters 359 in Figure 5b. Note that gLSTM uses K-hop aggregation here, whereas GCN does not; see Ap- 360 pendix D.7 for separated performance by aggregation strategy.

361 5.2 HOW DOES CAPACITY RELATE TO SENSITIVITY?

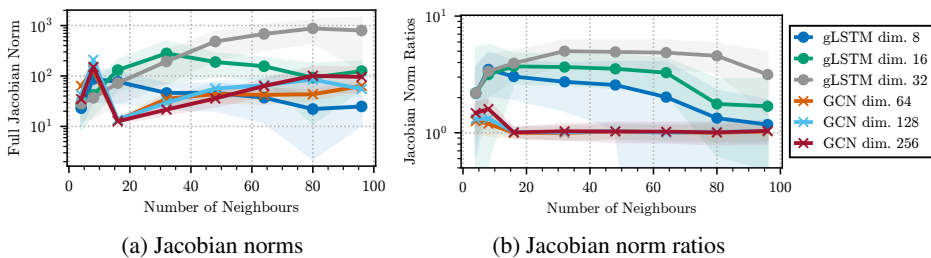
362 In this section, we investigate empirically how capacity over-squashing – as measured by perfor- 363 mance on NAR – relates to sensitivity over-squashing.

364 We directly measure the Jacobian norm of Topping et al. (2022); Di Giovanni et al. (2023a), 365 computing the sensitivity of the output feature vector on the central (output) node c to the input vectors 366 on the key-value neighbor nodes n , $|\partial \mathbf{h}_c^{(2)} / \partial \mathbf{x}_n|_{L_1}$. These results are visualized in Figure 6a.

367 We see therefore that sensitivity, as measured by the Jacobian norm, does not correlate with NAR 368 performance. Given that NAR performance degradation is due to capacity over-squashing, we there- 369 fore observe that **capacity over-squashing can occur without sensitivity over-squashing**. This is 370 clear from the fact that 1) sensitivity increases consistently for GCN models above $N = 16$ to the 371 point where it matches initial sensitivity, despite no increase in performance and 2) sensitivity for 372

378 gLSTM tends to carry on increasing beyond where performance starts to degrade. We note these
 379 trends – as with all observations we make in this section – hold true for the NAR regression task in
 380 Appendix D.8.1.

381 However, if we examine the difference in Jacobian norms between the neighbor nodes which are
 382 *selected* (those which have a key corresponding to the query node) vs *background*, we see trends that
 383 align with our notion of capacity. Figure 6a visualizes the ratio of Jacobian norms for selected nodes
 384 to that for background nodes. We observe that for all GCN models this ratio quickly falls to unity
 385 at the point where capacity over-squashing starts to occur, and gLSTM ratios consistently plateau –
 386 and start to slowly decrease – at their memory dimension, similarly coinciding with capacity over-
 387 squashing. It appears therefore that capacity over-squashing harms a model’s ability to be selectively
 388 sensitive to different nodes in the NAR task.



390 **Figure 6: Left:** Mean Jacobian norms for different gLSTM and GCN models, with varying number
 391 of neighbors in the NAR task. **Right:** Mean ratio between the Jacobian norms of the selected (key
 392 corresponds to query) to background (key is different from query) neighbor nodes, for varying model
 393 dimensions. Standard deviation shaded in both plots.

402 Another over-squashing sensitivity metric is that of Di Giovanni et al. (2023b), who introduce the
 403 *maximal mixing* metric. For node-level function $\mathbf{Y} : \mathbb{R}^{n \times d} \rightarrow \mathbb{R}^{n \times d}$, the mixing of features associated
 404 with nodes u, v at a given node i is defined as

$$\text{mix}(i, v, u) = \max_{\mathbf{Y}} \left\| \frac{\partial^2 (\mathbf{Y}(\mathbf{X}))_i}{\partial \mathbf{x}_u \partial \mathbf{x}_v} \right\|.$$

405 Although motivated through intuition of mixing, we observe the mixed partial derivative can equally
 406 be viewed as a composition of partial derivatives quantifying *selective sensitivity* - how much the
 407 sensitivity with respect to one node feature varies with respect to another node feature. In this
 408 respect, we expect it to be highly relevant to the sensitivity ratios visible in Figures 6b and 10.

409 To study this empirically for NAR, we take the maximum over the measured Hessians for different
 410 models. These Hessian 3-tensors are large, so we further limit to a subset of the overall tensor in
 411 order to compute them on available hardware: we are most interested in how the output sensitivity
 412 to the neighbor *value* vectors varies with the *query* vector, so we limit to the corresponding input
 413 dimensions. For the central, neighbor and query nodes c, n, q this adapted mixing metric is

$$\text{mix}(c, n, q) = \max_{\substack{0 \leq \alpha < N, \\ 0 \leq \beta < d_{\text{emb}}, \\ d_{\text{emb}} \leq \gamma < 2d_{\text{emb}}}} \left| \frac{\partial^2 (\mathbf{h}_c^{(2)})_\alpha}{\partial (\mathbf{x}_q)_\beta \partial (\mathbf{x}_n)_\gamma} \right|,$$

414 which we plot in Figure 7. We see that gLSTM consistently exhibits greater maximum Hessian
 415 values than GCN, and that this collapses for GCN models above 8 neighbors, consistent with the
 416 drop in performance. As with the Jacobian ratios, we see plateauing and slow decrease of maximum
 417 Hessian values above the memory dimension, but these trends are less pronounced.

418
 419
 420
 421
 422
 423
 424
 425
 426
 427
 428
 429
 430
 431

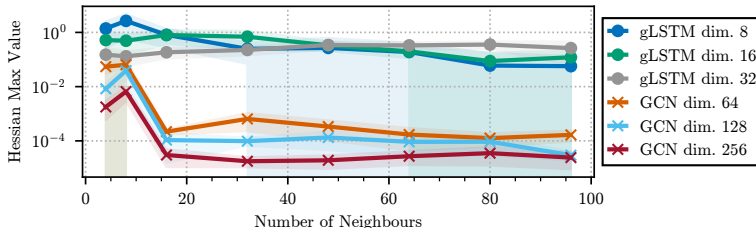


Figure 7: Mean of the maximum Hessian values for different gLSTM and GCN models, averaged across test set examples and different neighbor nodes. Standard deviation shaded.

5.3 LONG RANGE BENCHMARKS

Table 1: Mean and standard deviation of $\log_{10}(\text{MSE})$, averaged over 4 random weight initializations on the GPP tasks from Gravina et al. (2023), from which we report baselines. See Appendix D.1 for discussion of baseline choice. **Top** score in bold, second underlined. Lower is better.

Method	Diam.	Ecc.	SSSP
GCN	0.742 ± 0.047	0.846 ± 0.003	0.950 ± 0.000
GAT	0.822 ± 0.075	0.791 ± 0.022	0.695 ± 0.150
GraphSAGE	0.865 ± 0.40	0.286 ± 0.184	0.786 ± 0.021
GIN	0.613 ± 0.099	0.950 ± 0.001	-0.541 ± 0.419
GCNII	0.529 ± 0.057	0.764 ± 0.036	-1.132 ± 0.013
DGC	0.603 ± 0.005	0.826 ± 0.003	-0.148 ± 0.023
GRAND	0.672 ± 0.049	0.660 ± 0.139	-0.094 ± 0.340
A-DGN	-0.546 ± 0.033	0.305 ± 0.118	-3.402 ± 0.137
gLSTM (ours)	-0.715 ± 0.030	-4.036 ± 0.311	-2.836 ± 0.178
- K-hop	0.042 ± 0.123	0.673 ± 0.021	<u>-3.377 ± 0.142</u>

We evaluate gLSTM on the Graph Property Prediction (GPP) tasks from Gravina et al. (2023) and the Long Range Graph Benchmark (LRGB) from Dwivedi et al. (2022). These benchmarks are both designed to require long range interactions to solve, and thus are an interesting test of the ability of gLSTM to overcome over-squashing and over-smoothing in real world tasks in order to facilitate long range interactions. Performance is reported in Table 1 and Table 2 respectively.

gLSTM achieves comfortably state of the art results on the Diameter and Eccentricity GPP tasks, and very strong performance on SSSP; notably SSSP is the only tested task in which k-hop decreases performance. LRGB results show that gLSTM achieves strong performance in Peptides-Func but relatively weak performance on Peptides-Struct. We hypothesize that the weaker performance on Peptides-Struct may be due to long-range interactions being less relevant for this task, which is very effectively solved by a few-layer GCN. See Appendix D.2 for gLSTM ablations on these benchmarks and Appendix D.5 for details around hyperparameters used.

Table 2: Mean and standard deviation on LRGB (Dwivedi et al., 2022), averaged over four random weight initializations. Baselines from the LRGB reevaluation of Tönshoff et al. (2024), K-hop methods from Arroyo et al. (2025), rewiring baseline from Barbero et al. (2024b). All methods adhere to a 500k parameter limit. **Top** score in bold, second underlined.

Method	Peptides-Func		Peptides-Struct
	AP (\uparrow)	MAE (\downarrow)	
GCN	0.6860 ± 0.0050	0.2460 ± 0.0007	
GatedGCN	0.6765 ± 0.0047	0.2477 ± 0.0009	
GINE	0.6621 ± 0.0067	<u>0.2473 ± 0.0017</u>	
GPS	0.6534 ± 0.0091	0.2509 ± 0.0014	
<i>K-hop methods</i>			
kGCN-SSM	0.6902 ± 0.0022	0.2581 ± 0.0003	
DRew-GCN	0.6804 ± 0.0144	0.2766 ± 0.0019	
<i>Rewiring</i>			
LASER	0.6440 ± 0.0010	0.3043 ± 0.0019	
gLSTM (ours)	0.7250 ± 0.0023	0.2527 ± 0.0015	
- K-hop	0.6030 ± 0.0096	0.2638 ± 0.0010	

486 **6 CONCLUSION**
 487

488 In this work, we revisit over-squashing, disambiguating two bottleneck-related issues of sensitivity
 489 over-squashing and capacity over-squashing. We introduce a synthetic task that measures capacity
 490 over-squashing in isolation and we show that associative memory can improve MPNN capacity. The
 491 resulting architecture achieves strong results on real-world benchmarks.
 492

493 **Future Work** Many avenues remain open. Whereas the sensitivity issue of over-squashing has
 494 a mathematical basis via the node Jacobian, to our knowledge, the capacity issue does not. Theoretically
 495 quantifying this capacity could afford similar directions to those explored via sensitivity,
 496 establishing links to topology and model properties. With regards to architecture, we translate to a
 497 graph setting the gating and associative memory of xLSTM but do not retain the efficiency and par-
 498 allel training, leaving open future work on more efficient MPNNs: we highlight that the recent work
 499 of Pöppel et al. (2025) achieves these efficiency gains in the specific case of directed acyclic graphs.
 500 Another potential avenue would be to apply our findings to prevention of issues of over-mixing and
 501 representational collapse (Barbero et al., 2024a; 2025) in Transformer architectures.
 502

503 **REPRODUCIBILITY STATEMENT**
 504

505 We make available all of our code and experiment configurations to aid reproduction of results. Our
 506 experiments utilize the widely-used PyTorch Geometric GraphGym (You et al., 2020) framework
 507 which defines a standard framework for MPNN research.

508 For easiest reproduction of our results, please consult the `readme` in the code repository provided in
 509 Appendix D. The repository includes all necessary information to run the experiments: in particular,
 510 configs containing the hyperparameters used (also reported in Appendix D.5) and code for all plots
 511 used in the paper.
 512

513 **REFERENCES**
 514

515 Uri Alon and Eran Yahav. On the bottleneck of graph neural networks and its practical implications.
 516 In *International Conference on Learning Representations*, 2021.

517 Adrian Arnaiz-Rodriguez and Federico Errica. Oversmoothing, “oversquashing”, heterophily,
 518 long-range, and more: Demystifying common beliefs in graph machine learning. *arXiv preprint*
 519 *arXiv:2505.15547*, 2025.
 520

521 Simran Arora, Sabri Eyuboglu, Aman Timalsina, Isys Johnson, Michael Poli, James Zou, Atri
 522 Rudra, and Christopher Ré. Zoology: Measuring and improving recall in efficient language mod-
 523 els. In *Proceedings of 12th International Conference on Learning Representations (ICLR)*. ICLR,
 524 2024.

525 Álvaro Arroyo, Alessio Gravina, Benjamin Gutteridge, Federico Barbero, Claudio Gallicchio, Xi-
 526 aowen Dong, Michael Bronstein, and Pierre Vandergheynst. On vanishing gradients, over-
 527 smoothing, and over-squashing in gnns: Bridging recurrent and graph learning. *arXiv preprint*
 528 *arXiv:2502.10818*, 2025.
 529

530 Jimmy Ba, Geoffrey E Hinton, Volodymyr Mnih, Joel Z Leibo, and Catalin Ionescu. Using fast
 531 weights to attend to the recent past. *Advances in neural information processing systems*, 29,
 532 2016.

533 Federico Barbero, Andrea Banino, Steven Kapturowski, Dharshan Kumaran, João Madeira Araújo,
 534 Oleksandr Vitvitskyi, Razvan Pascanu, and Petar Veličković. Transformers need glasses! infor-
 535 mation over-squashing in language tasks. *Advances in Neural Information Processing Systems*,
 536 37:98111–98142, 2024a.
 537

538 Federico Barbero, Ameya Velingker, Amin Saberi, Michael M. Bronstein, and Francesco Di Gio-
 539 vanni. Locality-aware graph rewiring in GNNs. In *The Twelfth International Conference on*
Learning Representations, 2024b.

540 Federico Barbero, Alvaro Arroyo, Xiangming Gu, Christos Perivolaropoulos, Michael Bronstein,
 541 Petar Veličković, and Razvan Pascanu. Why do llms attend to the first token? *arXiv preprint*
 542 *arXiv:2504.02732*, 2025.

543

544 Maximilian Beck, Korbinian Pöppel, Markus Spanring, Andreas Auer, Oleksandra Prudnikova,
 545 Michael Kopp, Günter Klambauer, Johannes Brandstetter, and Sepp Hochreiter. xlstm: Extended
 546 long short-term memory. *Advances in Neural Information Processing Systems*, 37:107547–
 547 107603, 2024.

548 Maximilian Beck, Korbinian Pöppel, Phillip Lippe, Richard Kurle, Patrick M Blies, Günter Klam-
 549 bauer, Sebastian Böck, and Sepp Hochreiter. xLSTM 7b: A recurrent LLM for fast and efficient
 550 inference. In *Forty-second International Conference on Machine Learning*, 2025.

551

552 Mitchell Black, Zhengchao Wan, Amir Nayyeri, and Yusu Wang. Understanding oversquashing in
 553 gnns through the lens of effective resistance. In *International Conference on Machine Learning*,
 554 pp. 2528–2547. PMLR, 2023.

555 Xavier Bresson and Thomas Laurent. Residual gated graph convnets. *arXiv preprint*
 556 *arXiv:1711.07553*, 2017.

557

558 Joan Bruna, Wojciech Zaremba, Arthur Szlam, and Yann LeCun. Spectral networks and locally
 559 connected networks on graphs, 2014.

560

561 Gabriele Corso, Luca Cavalleri, Dominique Beaini, Pietro Liò, and Petar Veličković. Principal
 562 neighbourhood aggregation for graph nets. *Advances in neural information processing systems*,
 563 33:13260–13271, 2020.

564 Michaël Defferrard, Xavier Bresson, and Pierre Vandergheynst. Convolutional neural networks on
 565 graphs with fast localized spectral filtering, 2017.

566

567 Francesco Di Giovanni, Lorenzo Giusti, Federico Barbero, Giulia Luise, Pietro Lio, and Michael M
 568 Bronstein. On over-squashing in message passing neural networks: The impact of width, depth,
 569 and topology. In *International conference on machine learning*, pp. 7865–7885. PMLR, 2023a.

570

571 Francesco Di Giovanni, T Konstantin Rusch, Michael Bronstein, Andreea Deac, Marc Lackenby,
 572 Siddhartha Mishra, and Petar Veličković. How does over-squashing affect the power of gnns?
 573 *Transactions on Machine Learning Research*, 2024, 2023b.

574

575 Yuhui Ding, Antonio Orvieto, Bobby He, and Thomas Hofmann. Recurrent distance filtering for
 576 graph representation learning. In *International Conference on Machine Learning*, pp. 11002–
 577 11015. PMLR, 2024.

578

579 Vijay Prakash Dwivedi, Ladislav Rampášek, Michael Galkin, Ali Parviz, Guy Wolf, Anh Tuan
 580 Luu, and Dominique Beaini. Long range graph benchmark. *Advances in Neural Information
 Processing Systems*, 35:22326–22340, 2022.

581

582 Moshe Eliasof, Alessio Gravina, Andrea Ceni, Claudio Gallicchio, Davide Bacciu, and Carola-
 583 Bibiane Schönlieb. Grama: Adaptive graph autoregressive moving average models. *arXiv preprint*
 584 *arXiv:2501.12732*, 2025.

585

586 Federico Errica, Henrik Christiansen, Viktor Zaverkin, Takashi Maruyama, Mathias Niepert, and
 587 Francesco Alesiani. Adaptive message passing: A general framework to mitigate oversmooth-
 588 ing, oversquashing, and underreaching. In *Forty-second International Conference on Machine
 589 Learning*, 2025.

590

591 Ben Finkelshtein, Xingyue Huang, Michael Bronstein, and İsmail İlkan Ceylan. Cooperative graph
 592 neural networks. In *Proceedings of the 41st International Conference on Machine Learning*, pp.
 593 13633–13659, 2024.

594

595 Johannes Gasteiger, Stefan Weißenberger, and Stephan Günnemann. Diffusion improves graph
 596 learning. *Advances in neural information processing systems*, 32, 2019.

594 M Gori, G Monfardini, and F Scarselli. A new model for learning in graph domains. In *Proceedings.*
 595 *2005 IEEE International Joint Conference on Neural Networks, 2005.*, volume 2, pp. 729–734.
 596 IEEE, 2005.

597

598 Alessio Gravina, Davide Bacciu, Claudio Gallicchio, et al. Anti-symmetric dgn: a stable architecture
 599 for deep graph networks. In *Proceedings of the Eleventh International Conference on Learning*
 600 *Representations (ICLR 2023)*, 2023.

601 Alessio Gravina, Moshe Eliasof, Claudio Gallicchio, Davide Bacciu, and Carola-Bibiane Schönlieb.
 602 On oversquashing in graph neural networks through the lens of dynamical systems. In *Proceed-
 603 ings of the AAAI Conference on Artificial Intelligence*, volume 39, pp. 16906–16914, 2025.

604

605 Albert Gu and Tri Dao. Mamba: Linear-time sequence modeling with selective state spaces. *arXiv
 606 preprint arXiv:2312.00752*, 2023.

607 Benjamin Gutteridge, Xiaowen Dong, Michael M Bronstein, and Francesco Di Giovanni. Drew: Dy-
 608 namically rewired message passing with delay. In *International Conference on Machine Learning*,
 609 pp. 12252–12267. PMLR, 2023.

610

611 Will Hamilton, Zhitao Ying, and Jure Leskovec. Inductive representation learning on large graphs.
 612 *Advances in neural information processing systems*, 30, 2017.

613

614 Ali Hariri, Álvaro Arroyo, Alessio Gravina, Moshe Eliasof, Carola-Bibiane Schönlieb, Davide
 615 Bacciu, Kamyar Azizzadenesheli, Xiaowen Dong, and Pierre Vandergheynst. Return of cheb-
 616 net: Understanding and improving an overlooked gnn on long range tasks. *arXiv preprint
 617 arXiv:2506.07624*, 2025.

618 Simon Heilig, Alessio Gravina, Alessandro Trenta, Claudio Gallicchio, and Davide Bacciu. Port-
 619 hamiltonian architectural bias for long-range propagation in deep graph networks. In *The Thir-
 620 teenth International Conference on Learning Representations*, 2025.

621

622 Sepp Hochreiter and Jürgen Schmidhuber. Long short-term memory. *Neural computation*, 9(8):
 623 1735–1780, 1997.

624

625 John J Hopfield. Neural networks and physical systems with emergent collective computational
 626 abilities. *Proceedings of the national academy of sciences*, 79(8):2554–2558, 1982.

627

628 Weihua Hu, Matthias Fey, Marinka Zitnik, Yuxiao Dong, Hongyu Ren, Bowen Liu, Michele Catasta,
 629 and Jure Leskovec. Open graph benchmark: Datasets for machine learning on graphs. *Advances
 630 in neural information processing systems*, 33:22118–22133, 2020.

631

632 Samy Jelassi, David Brandfonbrener, Sham M Kakade, and Eran Malach. Repeat after me: Trans-
 633 formers are better than state space models at copying. In *International Conference on Machine
 634 Learning*, pp. 21502–21521. PMLR, 2024.

635

636 Angelos Katharopoulos, Apoorv Vyas, Nikolaos Pappas, and François Fleuret. Transformers are
 637 rnns: Fast autoregressive transformers with linear attention. In *International conference on ma-
 638 chine learning*, pp. 5156–5165. PMLR, 2020.

639

640 Thomas N. Kipf and Max Welling. Semi-supervised classification with graph convolutional net-
 641 works, 2017.

642

643 Alessio Micheli. Neural Network for Graphs: A Contextual Constructive Approach. *IEEE Trans-
 644 actions on Neural Networks*, 20(3):498–511, 2009.

645

646 Khang Nguyen, Nong Minh Hieu, Vinh Duc Nguyen, Nhat Ho, Stanley Osher, and Tan Minh
 647 Nguyen. Revisiting over-smoothing and over-squashing using ollivier-ricci curvature. In *In-
 648 ternational Conference on Machine Learning*, pp. 25956–25979. PMLR, 2023.

649

650 Antonio Orvieto, Samuel L Smith, Albert Gu, Anushan Fernando, Caglar Gulcehre, Razvan Pas-
 651 canu, and Soham De. Resurrecting recurrent neural networks for long sequences. In *International
 652 Conference on Machine Learning*, pp. 26670–26698. PMLR, 2023.

648 Oleg Platonov, Denis Kuznedelev, Michael Diskin, Artem Babenko, and Liudmila Prokhorenkova.
 649 A critical look at the evaluation of gnns under heterophily: Are we really making progress? *arXiv*
 650 *preprint arXiv:2302.11640*, 2023.

651

652 Korbinian Pöppel, Richard Freinschlag, Thomas Schmied, Wei Lin, and Sepp Hochreiter. pLSTM:
 653 parallelizable linear source transition mark networks. In *ICML 2025 Workshop on Long-Context*
 654 *Foundation Models*, 2025.

655 Ladislav Rampášek, Michael Galkin, Vijay Prakash Dwivedi, Anh Tuan Luu, Guy Wolf, and Do-
 656 minique Beaini. Recipe for a general, powerful, scalable graph transformer. *Advances in Neural*
 657 *Information Processing Systems*, 35:14501–14515, 2022.

658

659 Franco Scarselli, Marco Gori, Ah Chung Tsoi, Markus Hagenbuchner, and Gabriele Monfardini.
 660 The graph neural network model. *IEEE transactions on neural networks*, 20(1):61–80, 2008.

661

662 Imanol Schlag, Kazuki Irie, and Jürgen Schmidhuber. Linear transformers are secretly fast weight
 663 programmers. In *International conference on machine learning*, pp. 9355–9366. PMLR, 2021.

664

665 Jürgen Schmidhuber. Learning to control fast-weight memories: An alternative to dynamic recurrent
 666 networks. *Neural Computation*, 4(1):131–139, 1992.

667

668 Paul Smolensky. Tensor product variable binding and the representation of symbolic structures in
 669 connectionist systems. *Artificial intelligence*, 46(1-2):159–216, 1990.

670

671 Alessandro Sperduti. Encoding labeled graphs by labeling raam. *Advances in Neural Information*
 672 *Processing Systems*, 6, 1993.

673

674 Jan Tönshoff, Martin Ritzert, Eran Rosenbluth, and Martin Grohe. Where did the gap go? reassess-
 675 ing the long-range graph benchmark. *Transactions on Machine Learning Research*, 2024. ISSN
 676 2835-8856.

677

678 Jake Topping, Francesco Di Giovanni, Benjamin Paul Chamberlain, Xiaowen Dong, and Michael M.
 679 Bronstein. Understanding over-squashing and bottlenecks on graphs via curvature. In *Inter-
 680 national Conference on Learning Representations*, 2022.

681

682 Ashish Vaswani, Noam Shazeer, Niki Parmar, Jakob Uszkoreit, Llion Jones, Aidan N Gomez,
 683 Łukasz Kaiser, and Illia Polosukhin. Attention is all you need. *Advances in neural informa-
 684 tion processing systems*, 30, 2017.

685

686 Petar Veličković, Guillem Cucurull, Arantxa Casanova, Adriana Romero, Pietro Liò, and Yoshua
 687 Bengio. Graph attention networks. *ArXiv*, 2018.

688

689 Keyulu Xu, Weihua Hu, Jure Leskovec, and Stefanie Jegelka. How powerful are graph neural
 690 networks? *arXiv preprint arXiv:1810.00826*, 2018.

691

692 Jiaxuan You, Rex Ying, and Jure Leskovec. Design space for graph neural networks. In *NeurIPS*,
 693 2020.

694

695

696

697

698

699

700

701

702 A RELATIONSHIP TO COMPUTATIONAL (AND TOPOLOGICAL)
 703 BOTTLENECKS
 704

705 Arnaiz-Rodriguez & Errica (2025) identify a separation in the over-squashing literature between the
 706 initial work of Alon & Yahav (2021) and the later work of Topping et al. (2022); Di Giovanni et al.
 707 (2023a). They point out that the original over-squashing definition of (Alon & Yahav, 2021) was
 708 associated with the computational tree, and Topping et al. (2022) later connected over-squashing
 709 to the existence of topological bottlenecks. They suggest that these definitions constitute different
 710 problems, and that – as a community – we should discard the term “over-squashing” and separate it
 711 into (at least) two separate terms: (1) computational tree bottlenecks and (2) topological bottlenecks
 712 (in the underlying graph).

713 This makes a valuable point: topological bottlenecks may or may not be involved when structural
 714 issues exist with the computational tree. The authors fairly point out that the umbrella term “over-
 715 squashing” has sometimes hidden some of the complexity of the problem, and the field may ben-
 716 efit from work identifying explicitly whether it is dealing with topological bottlenecks (as is the
 717 case with e.g. rewiring) or bottlenecks of the computational tree (e.g. adaptive message passing).
 718 We’re unsure that framing these as *separate* is helpful, since topological bottlenecks must be me-
 719 diated through the computational tree in order to impact message passing, but the point stands that
 720 some methods to combat over-squashing specifically target topological bottlenecks (and as such any
 721 changes to the computational graph are implicit), and some methods target general computational
 722 bottlenecks, and that this is not always clear.

723 Despite the complexity, we believe the term “over-squashing” still has utility as an umbrella term that
 724 describes issues that arise from the presence of bottlenecks and depth in the computational tree. The
 725 distinction made by Arnaiz-Rodriguez & Errica (2025) clarifies that sometimes these issues arise
 726 due to topological bottlenecks in the underlying graph, and sometimes they do not. The relevance
 727 of our work is then in exploring *how* this structure manifests as performance issues, and the main
 728 body of our paper argues that this is due to separate issues of **capacity** and **sensitivity**.

729 Precisely *how* issues of capacity and sensitivity relate to the structure of the computational tree and
 730 the presence of bottlenecks is complex, although we take initial steps to clarify this in our paper.
 731 It would **not** be correct to suggest for example that capacity issues correspond to computational
 732 bottlenecks and low sensitivity to topological bottlenecks. In particular:

- 733 • Our RingTransfer discussion of Section 3.1 highlights that computational bottlenecks can
 734 exist without capacity issues.
- 735 • Arnaiz-Rodriguez & Errica (2025) highlight that low sensitivity does not necessarily imply
 736 the existence of computational tree bottlenecks (or topological bottlenecks).
- 737 • On the other hand, both topological bottlenecks and general computational bottlenecks
 738 can cause low sensitivity. This is clear since the Equation (3) defines an upper bound on
 739 sensitivity in terms of the computational tree (defined by successive powers of the message-
 740 passing matrix), and we refer the reader to the work of Topping et al. (2022) for proofs in
 741 the case of specifically topological bottlenecks.

742 Additionally, while the discussion in this Appendix has so far focused on the computational tree, we
 743 highlight that the causes of the failure modes discussed in our work extend beyond structural issues:
 744 issues of capacity also depend at least on (1) information content of the task and (2) storage capacity
 745 of the model, as explored in Sections 3.1 and 3.2 respectively, and issues of sensitivity are highly
 746 dependent on the model dynamics, as explored in e.g. Arroyo et al. (2025); Heilig et al. (2025);
 747 Gravina et al. (2023; 2025).

750 B xLSTM UPDATE EQUATIONS
 751

752 Beck et al. (2024) initially designed xLSTM as a combination of sLSTM blocks and mLSTM blocks
 753 - using scalar memory and matrix (associative) memory respectively. However, their follow up work
 754 (Beck et al., 2025) uses only mLSTM blocks, and these form the inspiration for gLSTM. Therefore,
 755 we will exclusively introduce the mLSTM block update equations in this section.

756 The update equations, presented in a similar manner to Section 4, are given below.
 757
 758 **State (and normalization) updates:**

$$C^t = f^t C^{t-1} + i^t \mathbf{v}^t \otimes \mathbf{k}^t \quad (4)$$

$$\mathbf{n}^t = f^t \mathbf{n}^{t-1} + i^t \mathbf{k}^t \quad (5)$$

$$m^t = \max \left(\tilde{f}^t + m^{t-1}, \tilde{i}^t \right) \quad (6)$$

764 **Query / Key / Value computation:**
 765

$$\mathbf{q}^t = \mathbf{W}_q \mathbf{x}^t + \mathbf{b}_q \quad (7)$$

$$\mathbf{k}^t = \frac{1}{\sqrt{d}} \mathbf{W}_k \mathbf{x}^t + \mathbf{b}_k \quad (8)$$

$$\mathbf{v}^t = \mathbf{W}_v \mathbf{x}^t + \mathbf{b}_v \quad (9)$$

771 **Gate computation:**
 772

$$i^t = \exp \left(\tilde{i}^t - m^t \right) \quad \tilde{i}^t = \mathbf{w}_i^T \mathbf{x}^t + b_i \quad (10)$$

$$f^t = \exp \left(\tilde{f}^t + m^{t-1} - m^t \right) \quad \tilde{f}^t = \mathbf{w}_f^T \mathbf{x}^t + b_f \quad (11)$$

$$\mathbf{o}^t = \sigma(\tilde{\mathbf{o}}^t) \quad \tilde{\mathbf{o}}^t = \mathbf{W}_o \mathbf{x}^t + \mathbf{b}_o \quad (12)$$

778 **Output:**
 779

$$\tilde{\mathbf{h}}^t = \mathbf{C}^t \mathbf{q}^t / \max \left\{ |\mathbf{n}^{t T} \mathbf{q}^t|, 1 \right\} \quad (13)$$

$$\mathbf{h}^t = \mathbf{o}^t \odot \tilde{\mathbf{h}}^t \quad (14)$$

783 C DATASET DETAILS

785 In table Table 3 we present a summary of the statistics of the datasets used throughout this work.
 786 We use the standard splits provided for each of the datasets, using the standard loading functionality
 787 from GraphGym (and PyTorch Geometric). For GPP (without a default implementation in PyTorch
 788 Geometric) we use the original splits of Gravina et al. (2023): 5120 graphs as training set, 640 as
 789 validation set, and 1280 as test set.
 790

791 For the NAR task (for all neighbor values), we use a split of 8,000 train graphs, 1,000 validation
 792 graphs and 1,000 test graphs. We note that when testing gLSTM on this dataset, we vary the memory
 793 (matrix) dimension as described in the main text, and set the vector dimension to twice that of the
 794 matrix dimension.
 795

796 D ADDITIONAL EXPERIMENTS

798 Our code for reproducing all experimental results in the main paper and appendices is publicly
 799 available at <https://anonymous.4open.science/r/GNN-xLSTM-9A2D>.

801 D.1 ADDITIONAL GPP BASELINES

803 We note that due to a subtle PyTorch issue in the original GPP code implementation, normalization
 804 is not applied to the dataset targets. A refactor appears to have unknowingly fixed this issue in later
 805 iterations of the code so later experiments are run on a normalized variant of the dataset. Unfor-
 806 tunately, this results in unfair comparison, as results can be substantially different between the two
 807 variants of the dataset.

808 Therefore, in the main body of the paper we test only on the baselines provided in the original GPP
 809 paper (Gravina et al., 2023), as we are confident these use the un-normalized variant of the dataset,
 and this provides us with the largest number of baselines to test against. We additionally ensure that

810
 811 Table 3: Summary of datasets used throughout this work. Node and edge values are the average per
 812 graph, where applicable. LRGB statistics retrieved from Dwivedi et al. (2022), OGB statistics from
 813 Hu et al. (2020), Heterophilous from Platonov et al. (2023). GPP statistics computed; dataset from
 814 Gravina et al. (2023); Corso et al. (2020).

Dataset	Group	Task	Setting	#Graphs	Nodes	Edges
Peptides-Func	LRGB	Graph cls.	Inductive	15,535	150.94	307.30
Peptides-Struct	LRGB	Graph reg.	Inductive	15,535	150.94	307.30
Diameter	GPP	Graph reg.	Inductive	7,040	28.82	98.95
Eccentricity	GPP	Node reg.	Inductive	7,040	28.82	98.95
SSSP	GPP	Node reg.	Inductive	7,040	28.82	98.95
arXiv	OGB	Node cls.	Transductive	1	169,343	1,166,243
Products	OGB	Node cls.	Transductive	1	2,449,029	61,859,140
Amazon-Ratings	Heterophilous	Node cls.	Transductive	1	24,492	93,050
Roman-Empire	Heterophilous	Node cls.	Transductive	1	22,662	32,927
Minesweeper	Heterophilous	Node cls.	Transductive	1	10,000	39,402

815
 816
 817
 818
 819
 820
 821
 822
 823
 824
 825
 826
 827
 828 our method uses the same, un-normalized GPP variant. We separately test on the normalized version
 829 of the dataset, with results presented in Table 4 and hyperparameters in Table 14. This allows us
 830 to additionally test against a range of more recent methods that specifically target sensitivity over-
 831 squashing. We achieve state of the art results on the normalized variant of this benchmark.
 832

833 Table 4: Mean and standard deviation of $\log_{10}(\text{MSE})$, averaged over 4 random weight initializations
 834 on the Normalized version of the GPP tasks from Gravina et al. (2023). Baselines reported from
 835 Arroyo et al. (2025); Eliasof et al. (2025). **Top** score in bold. Lower is better.
 836

Method	Diam.	Ecc.	SSSP
<i>Differential Equation Inspired GNNs</i>			
SWAN	-0.598 ± 0.115	-0.074 ± 0.219	-3.543 ± 0.083
PH-DGN	-0.547 ± 0.107	-0.935 ± 0.210	-4.299 ± 0.072
<i>K-hop methods</i>			
DRew-GCN	-2.402 ± 0.110	-2.029 ± 0.024	-1.602 ± 0.008
kGCN-SSM	-3.075 ± 0.055	-4.265 ± 0.178	-3.604 ± 0.029
GPS	-0.512 ± 0.043	0.608 ± 0.028	-3.599 ± 0.195
GRAMA	-0.866 ± 0.051	-1.301 ± 0.126	-3.935 ± 0.070
gLSTM (ours)	-3.684 ± 0.057	-5.912 ± 1.116	-5.321 ± 0.603

849 850 D.2 ABLATIONS

851 To identify what elements of the gLSTM architecture are most important for performance on these
 852 benchmarks, we perform ablations on the GPP and LRGB datasets. For LRGB, a task with a parameter
 853 limit, we ablate in two different settings: the first is simply removing the ablated component,
 854 for which results are presented in Table 6. The second is to scale the hidden dimension h to keep
 855 the parameter count as close as possible to the 500k limit - i.e. when removing gating, this will
 856 correspondingly increase the hidden dimension. We include these experiments as they more accurately
 857 represent the reality of testing a model variant on a task with a parameter limit; these results
 858 are presented in Table 7. These two ablation settings show very similar results. GPP ablations are
 859 presented in Table 5.

860 We see that ablating gating only significantly reduces performance on Peptides-Func - other than
 861 this, it either leaves performance the same or in some cases, improves performance (GPP Ecc. in
 862 particular).

864

865

866 Table 5: Ablation of gLSTM performance on Diam, Ecc, and SSSP from the GPP benchmark. Mean
 867 and standard deviation are reported, averaged over four random weight initializations. Other than
 868 ablation, all other model settings are held constant; thus ablations with gating removed have reduced
 869 parameter count.

870

Model	Diam.	Ecc.	SSSP
gLSTM	-0.715 ± 0.030	-4.036 ± 0.311	-2.836 ± 0.178
- Output gate	-0.70 ± 0.05	-3.71 ± 0.16	-2.77 ± 0.19
- Input gate	-0.75 ± 0.01	-4.72 ± 0.36	-3.27 ± 0.16
- Forget gate	-0.71 ± 0.03	-4.30 ± 0.21	-3.14 ± 0.07
- All gates	-0.75 ± 0.03	-4.14 ± 0.42	-3.16 ± 0.15
- K-hop aggregation	0.04 ± 0.12	0.67 ± 0.02	-3.38 ± 0.14

871

872

873

874

875

876

877

878

879

880

881

882

883

884

885

886

Table 6: Ablation of gLSTM performance on Peptides-Func and Peptides-Struct from the LRGB. Mean and standard deviation are reported, averaged over four random weight initializations. Other than ablation, all other model settings are held constant; thus ablations with gating removed have reduced parameter count.

887

888

889

890

891

892

893

894

895

896

897

898

899

900

901

Table 7: Ablation of gLSTM performance on Peptides-Func and Peptides-Struct from the LRGB. Mean and standard deviation are reported, averaged over four random weight initializations. All methods adhere to a 500k parameter limit such that hidden dimension varies to keep parameter count as close to this as possible.

902

903

904

905

906

907

908

909

910

911

912

913

914

915

916

917

Model	Peptides-Func	Peptides-Struct
	AP (\uparrow)	MAE (\downarrow)
gLSTM	0.7250 ± 0.0023	0.2527 ± 0.0015
- Output gate	0.7086 ± 0.0049	0.2540 ± 0.0016
- Input gate	0.7186 ± 0.0029	0.2524 ± 0.0027
- Forget gate	0.7236 ± 0.0063	0.2522 ± 0.0011
- All gates	0.7180 ± 0.0088	0.2526 ± 0.0012
- Positional encoding	0.7208 ± 0.0072	0.2539 ± 0.0036
- K-hop aggregation	0.6030 ± 0.0096	0.2638 ± 0.0010

Model	Peptides-Func	Peptides-Struct
	AP (\uparrow)	MAE (\downarrow)
gLSTM	0.7250 ± 0.0023	0.2527 ± 0.0015
- Output gate	0.7202 ± 0.0056	0.2537 ± 0.0011
- Input gate	0.7193 ± 0.0110	0.2518 ± 0.0027
- Forget gate	0.7148 ± 0.0107	0.2545 ± 0.0043
- All gates	0.7188 ± 0.0060	0.2528 ± 0.0035
- Positional encoding	0.7211 ± 0.0062	0.2601 ± 0.0017
- K-hop aggregation	0.6030 ± 0.0096	0.2638 ± 0.0010

Table 8: Mean and standard deviation on Heterophilic Datasets, averaged over four random weight initializations.

Model	Roman-empire	Amazon-ratings	Minesweeper
	Acc \uparrow	Acc \uparrow	AUC \uparrow
MPNNs			
GAT	80.87 \pm 0.30	49.09 \pm 0.63	92.01 \pm 0.68
GAT (LapPE)	84.80 \pm 0.46	44.90 \pm 0.73	93.50 \pm 0.54
GAT (RWSE)	86.62 \pm 0.53	48.58 \pm 0.41	92.53 \pm 0.65
Gated-GCN	74.46 \pm 0.54	43.00 \pm 0.32	87.54 \pm 1.22
GCN	73.69 \pm 0.74	48.70 \pm 0.63	89.75 \pm 0.52
GCN (LapPE)	83.37 \pm 0.55	44.35 \pm 0.36	94.26 \pm 0.49
GCN (RWSE)	84.84 \pm 0.55	46.40 \pm 0.55	93.84 \pm 0.48
CO-GNN(Σ, Σ)	91.57 \pm 0.32	51.28 \pm 0.56	95.09 \pm 1.18
CO-GNN(μ, μ)	91.37 \pm 0.35	54.17 \pm 0.37	97.31 \pm 0.41
SAGE	85.74 \pm 0.67	53.63 \pm 0.39	93.51 \pm 0.57
Graph Transformers			
Exphormer	89.03 \pm 0.37	53.51 \pm 0.46	90.74 \pm 0.53
NAGphormer	74.34 \pm 0.77	51.26 \pm 0.72	84.19 \pm 0.66
GOAT	71.59 \pm 1.25	44.61 \pm 0.50	81.09 \pm 1.02
GPS	82.00 \pm 0.61	53.10 \pm 0.42	90.63 \pm 0.67
GPS _{GCN+Performer} (LapPE)	83.96 \pm 0.53	48.20 \pm 0.67	93.85 \pm 0.41
GPS _{GCN+Performer} (RWSE)	84.72 \pm 0.65	48.08 \pm 0.85	92.88 \pm 0.50
GPS _{GCN+Transformer} (LapPE)	OOM	OOM	91.82 \pm 0.41
GPS _{GCN+Transformer} (RWSE)	OOM	OOM	91.17 \pm 0.51
GT	86.51 \pm 0.73	51.17 \pm 0.66	91.85 \pm 0.76
GT-sep	87.32 \pm 0.39	52.18 \pm 0.80	92.29 \pm 0.47
Polynormer	92.55 \pm 0.30	54.81 \pm 0.49	97.46 \pm 0.36
Heterophily-Designated GNNs			
CPGNN	63.96 \pm 0.62	39.79 \pm 0.77	52.03 \pm 5.46
FAGCN	65.22 \pm 0.56	44.12 \pm 0.30	88.17 \pm 0.73
FSGNN	79.92 \pm 0.56	52.74 \pm 0.83	90.08 \pm 0.70
GBK-GNN	74.57 \pm 0.47	45.98 \pm 0.71	90.85 \pm 0.58
GloGNN	59.63 \pm 0.69	36.89 \pm 0.14	51.08 \pm 1.23
GPR-GNN	64.85 \pm 0.27	44.88 \pm 0.34	86.24 \pm 0.61
H2GCN	60.11 \pm 0.52	36.47 \pm 0.23	89.71 \pm 0.31
JacobiConv	71.14 \pm 0.42	43.55 \pm 0.48	89.66 \pm 0.40
Graph SSMs			
GMIN	87.69 \pm 0.50	54.07 \pm 0.31	91.01 \pm 0.23
GPS + Mamba	83.10 \pm 0.28	45.13 \pm 0.97	89.93 \pm 0.54
GRAMAGCN	88.61 \pm 0.43	53.48 \pm 0.62	95.27 \pm 0.71
MP-SSM	90.91 \pm 0.48	53.65 \pm 0.71	95.33 \pm 0.72
Ours			
gLSTM (ours)	88.12 \pm 0.35	51.98 \pm 0.45	92.08 \pm 0.88
+ K-hop	83.48 \pm 0.30	52.25 \pm 0.31	87.55 \pm 0.78

D.3 HETEROGRAPHIC BENCHMARKS

We additionally evaluate gLSTM on the heterophilic datasets of Platonov et al. (2023), shown in Table 8. Hyperparameters and sweeps are documented in Appendix D.5 (Table 13).

gLSTM achieves good MPNN-level performance, but is outperformed by some Graph Transformer architectures. Notably, the addition of K-hop aggregation here actually *harms* performance significantly in two of the three datasets. We suggest this may be due in part to the lack of long-range dependencies in these datasets, whereas the GPP and LRGB datasets evaluated in the main text are designed specifically to contain long range dependencies. This explanation would imply that K-hop provides a useful inductive bias for long range dependencies specifically.

Table 9: Mean and standard deviation on OGBN, averaged over four random weight initializations.

Method	Arxiv	Products
GCN	71.74 ± 0.29	75.64 ± 0.21
ChebNet	73.27 ± 0.23	-
ChebNetII	72.32 ± 0.23	-
GraphSAGE	71.49 ± 0.27	78.29 ± 0.16
GAT	72.02 ± 0.44	79.45 ± 0.59
NodeFormer	59.90 ± 0.42	72.93 ± 0.13
GraphGPS	70.97 ± 0.41	OOM
GOAT	72.41 ± 0.40	82.00 ± 0.43
NAGphormer	70.13 ± 0.55	73.55 ± 0.21
Exphormer	72.44 ± 0.28	OOM
SGFormer	72.63 ± 0.13	74.16 ± 0.31
Polynormer	73.46 ± 0.16	83.82 ± 0.11
gLSTM (ours)	71.91 ± 0.32	81.52 ± 0.29

D.4 LARGE GRAPH BENCHMARKS AND SCALING EXPERIMENTS

This section investigates the scaling of gLSTM to large graphs, for which we use the Arxiv and Products node classification datasets from the Open Graph Benchmark (Hu et al., 2020). `ogbn-arxiv` comprises 169,343 nodes and 1,166,243 edges, while `ogbn-products` comprises 2,449,029 nodes and 61,859,140 edges. We evaluate gLSTM on these graphs without K-hop aggregation, which would be prohibitively expensive to compute on these graphs. However, as noted in Appendix D.3, it appears that K-hop aggregation is of particular importance for long-range dependencies, so it is unclear whether it would improve performance on these benchmarks anyway.

Results on these datasets are presented in Table 9. Hyperparameters and sweeps are documented in Appendix D.5 (Table 12).

We highlight that although the model which achieves best validation-set performance on `ogbn-arxiv` is large, thus incurring high runtime and VRAM usage, significantly smaller models achieve comparable results with only a small decrease in accuracy: in particular, a model with memory dimension 8, 8 heads and 4 layers achieves an accuracy of 71.31 ± 0.25 .

We use `ogbn-arxiv` to empirically measure gLSTM epoch time and VRAM scaling with the number of heads and memory dimension: these results are visualized in Figure 8, reporting both absolute values and multiples of the corresponding metric for a GCN model with 4 layers and hidden dimension 256 on the same dataset. As expected, these values appear to scale linearly with the number of heads and quadratically with the (matrix) memory dimension.

We highlight that we have not optimized any of the gLSTM code for CUDA efficiency, so the relative epoch times and VRAM usages may be overstated, and future improvements are likely possible.

D.5 HYPERPARAMETERS

In Tables 10 and 11 we present the hyperparameter sweeps and chosen hyperparameters for results in the main body of the paper: GPP and LRGB respectively. In Tables 12 to 14 we present the hyperparameter sweeps and chosen hyperparameters for the normalized version of GPP (Appendix D.1), Heterophilic benchmarks (Appendix D.3) and OGBN benchmarks (Appendix D.4) respectively.

D.6 OVERSMOOTHING AND LONG RANGE DEPENDENCIES

We test empirically that gLSTM is able to learn long range dependencies by evaluating on the RingTransfer task introduced in Di Giovanni et al. (2023a). Results for gLSTM, GCN and GNN-SSM (Arroyo et al., 2025) are shown for various ring sizes (and corresponding number of message passing layers) in Figure 9.

1026
10271028 Table 10: Hyperparameter sweeps for gLSTM on LRGB tasks. In bold are the hyperparameters
1029 that achieved the best validation set performance, and thus were those used in the main results of
1030 the paper. Note that hidden dimension was not directly swept over, as this was maximized for each
1031 configuration such that the model remained within the 500k parameter budget. Due to compute
1032 limitations, hyperparameter sweeps were not exhaustive, but used *Weights and Biases* Bayesian
1033 Optimization routine with Hyperband early termination.

1034

Hyperparameter	Peptides-Func	Peptides-Struct
Memory Dimension	8, 16, 32	8, 16 , 32
Number of Heads	1-2-8	1- 5 -8
Message Passing Layers	10- 27 -50	4- 23 -40
Input Norm Type	Layer	Layer , None
Hidden Norm Type	Group	Group
Act. Func. (between block)	GeLU, ReLU, None	GeLU, ReLU , None
Dropout	0.1	0.0 , 0.1, 0.2
Hidden Dimension	45	42

1044

1045

1046

1047

1048

1049

1050

Table 11: Hyperparameter sweeps for gLSTM on GPP tasks. In bold are the hyperparameters that
achieved the best validation set performance, and thus were those used in the main results of the
paper. Hyperparameters were tested exhaustively via grid search.

1051

Hyperparameter	Diam.	Ecc.	SSSP
Memory Dimension	8, 16	8 , 16	8, 16
Number of Heads	1, 2, 3, 4	1, 2, 3, 4	1, 2, 3, 4
Message Passing Layers	1, 5, 10, 20	1, 5, 10 , 20	1, 5, 10 , 20
Input Norm Type	None	None	None
Hidden Norm Type	Group	Group	Group
Act. Func. (between block)	Tanh, ReLU, None	Tanh, ReLU , None	Tanh, ReLU, None
Dropout	0.0	0.0	0.0
Hidden Dimension	10 , 20, 30	10, 20 , 30	10, 20, 30

1061

1062

1063

1064

1065

1066

1067

Table 12: Hyperparameter sweeps for gLSTM on OGBN (Hu et al., 2020) tasks. Bold entries
indicate the hyperparameters that achieved the best validation performance and were used in the
main experiments.

1068

1069

1070

1071

1072

1073

1074

1075

1076

1077

1078

1079

Hyperparameter	ogbn-arxiv	ogbn-products
Memory Dimension	8,16, 32	8 ,16,32
Number of Heads	4 ,8	4 ,8
Message Passing Layers	4,6,8,10	4,6,8,10
Input Norm Type	Batch	Layer
Hidden Norm Type	Group	Group
Act. Func. (between block)	ReLU	ReLU
Dropout	0.5	0.5
Hidden Dimension	256	

1080
1081
1082
1083
1084
1085
1086
1087
1088
1089

Table 13: Hyperparameter sweeps for gLSTM on the heterophilous datasets of Platonov et al. (2023). Bold entries indicate the hyperparameters selected based on validation performance. Sweep ranges were identical across datasets.

Hyperparameter	Amazon Ratings	Minesweeper	Roman Empire
Memory Dimension	8,16,32	8,16,32	8,16,32
Number of Heads	4,8	4,8	4,8
Message Passing Layers	4,6,8,10,12	4,6,8,10,12	4,6,8,10,12
Input Norm Type	Batch	Batch	Batch
Hidden Norm Type	Group	Group	Group
Act. Func. (between block)	ReLU	ReLU	ReLU
Dropout	0.5	0.2	0.5
Hidden Dimension	512	64	512

1100
1101
1102
1103
1104
1105
1106
1107
1108
1109
1110
1111
1112
1113

Table 14: Hyperparameter sweeps for gLSTM on the Normalized-GPP tasks: sweep is performed only over Normalized-Diam and these parameters are used for all other experiments. In bold are the hyperparameters that achieved the best validation set performance, and thus were those used for test set evaluation.

Hyperparameter	Normalized-Diam.
Memory Dimension	8, 16, 32
Number of Heads	1-4-8
Message Passing Layers	4-10-40
Input Norm Type	Layer
Hidden Norm Type	Group
Act. Func. (between block)	GeLU, ReLU, None
Dropout	0.0 0.1 0.2
Hidden Dimension	512

1128
1129
1130
1131
1132
1133

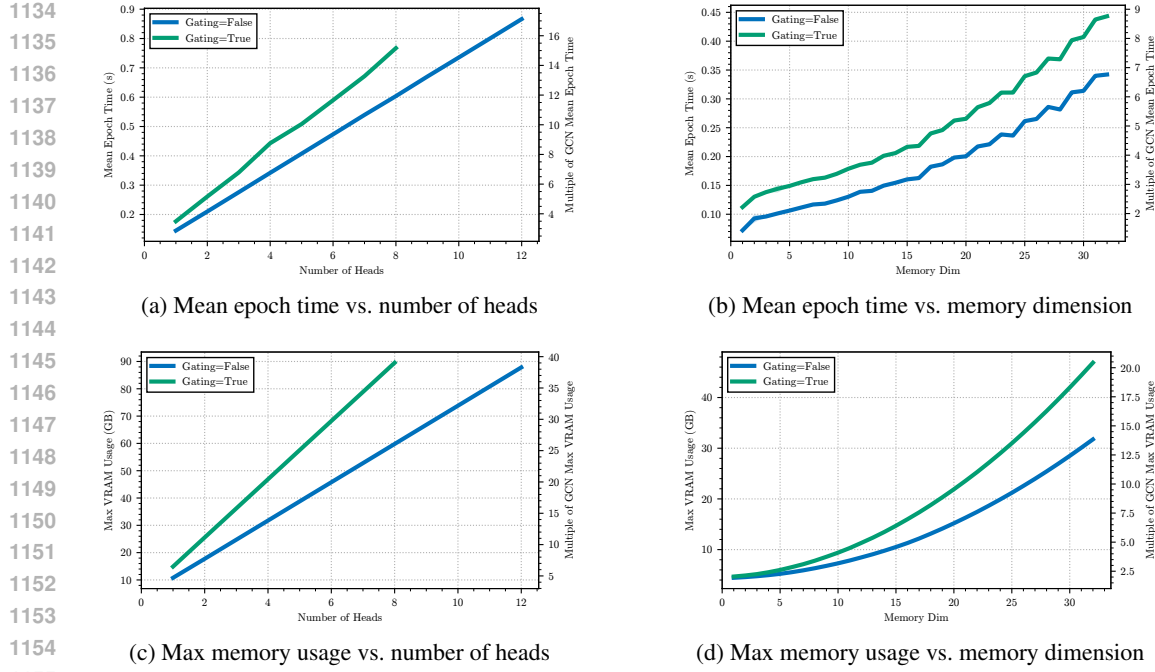


Figure 8: Scaling behavior of gLSTM, empirically reported on the `ogbn-arxiv` dataset (Hu et al., 2020). Mean epoch time and max memory usage is reported, both in absolute terms and relative to GCN with 4 layers and hidden dimension of 256. All parameters other than that being varied are fixed to that of the top-performing model: see Table 12.

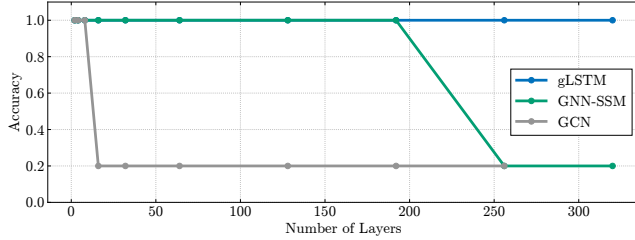


Figure 9: Performance on the RingTransfer task.

D.7 ADDITIONAL NAR CLASSIFICATION RESULTS

In this section, we present various additional results from the NAR task presented in the main body of the paper.

We visualize the Jacobian norms - separated by selected vs background nodes - for the mixed aggregation strategies used in the main paper in Figure 10. This is, in effect, the more granular plot of Figure 6b.

D.7.1 COMPARISON AGAINST (GRAPH) TRANSFORMER BASELINES

In addition to the MPNN comparisons presented in the main body of the paper and Appendix D.7.3, we compare gLSTM against two Transformer baselines: GraphGPS (Rampášek et al., 2022) and a regular Transformer (Vaswani et al., 2017) block utilizing softmax attention. These results are visualized in Figure 11.

From this figure, we see that softmax attention with a sufficiently high hidden dimension is able to solve the task perfectly, as expected. Curiously, GraphGPS fails significantly earlier, at 32 neighbors for all hidden dimensions tested: while we unsure of the precise reason for this, we speculate that

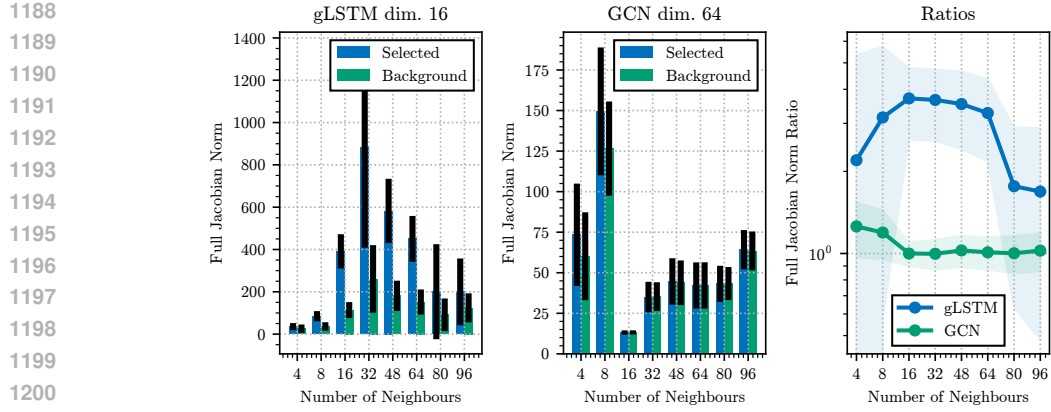


Figure 10: **Left:** Mean Jacobian norms for gLSTM of memory dimension 16, with varying number of neighbors in the NAR task, separated by whether the neighbor node corresponds to the given query (selected) or not (background). **Middle:** Same, with GCN of hidden dimension 64. **Right:** Mean ratios of Jacobian norms for selected nodes to background nodes, for these two models. Standard deviation visualized in bar chart error bars and line chart shaded area.

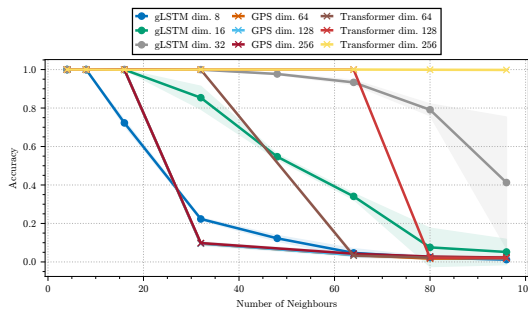


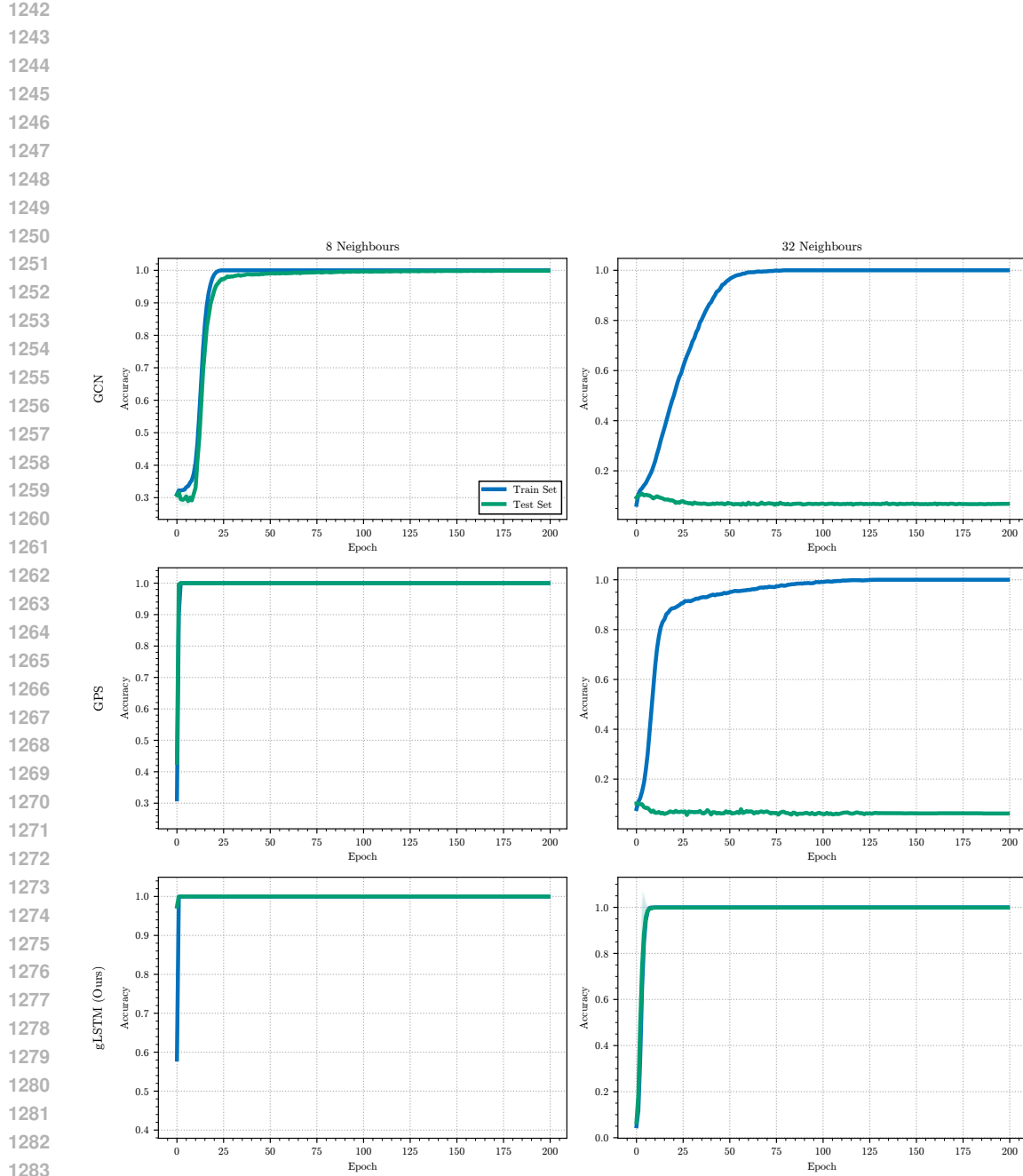
Figure 11: Comparison of gLSTM performance against Transformer baselines: GPS (Rampášek et al., 2022) and a standard Transformer baseline with softmax attention. Both of these use Laplacian positional encodings appended to the node feature vectors. Test-set mean accuracy is shown, with standard deviation shaded, averaged over 3 runs. Note that gLSTM uses K-hop aggregation here, whereas GPS does not.

the GCN aspect of the architecture may be actively harming performance. We note however that GraphGPS does outperform all MPNNs tested, other than gLSTM.

It is also interesting to note that at lower dimensions, softmax attention reaches a neighbor count at which it also starts to fail. It seems clear that this arises simply from the initial embedding of the integer key, query and value symbols: when the size of these alphabets exceeds half the hidden dimension (recall half of the embedding vector is used to encode the key, the other half the query), it is no longer possible for each symbol to have a learned orthogonal vector and there will be overlap.

D.7.2 TRAINING CURVES: FAILURE AT NAR IS AN ISSUE OF GENERALIZATION

This section investigates further what exactly causes GCN and other models to fail at NAR. We observe in Figure 12 that for several models, above the point where test set accuracy decreases, train set accuracy remains high: thus, the failure mode seems to be one of *generalization*. We suggest that this is consistent with the capacity intuition: at the point at which the model is no longer able to separably store the neighbor representations, it collapses instead to memorizing the aggregated neighbor representation and corresponding value. Since these specific combinations are not shared with the test set, this does not generalize.



1284 Figure 12: Train and test set accuracies plotted against epoch count. Left column contains the results
1285 for experiments using 8 neighbor nodes, right column for 32 neighbors. Top row visualises GCN
1286 results, second GPS, third gLSTM. gLSTM is the only one that remains able to generalize at 32
1287 neighbors (and beyond).

1288
1289
1290
1291
1292
1293
1294
1295

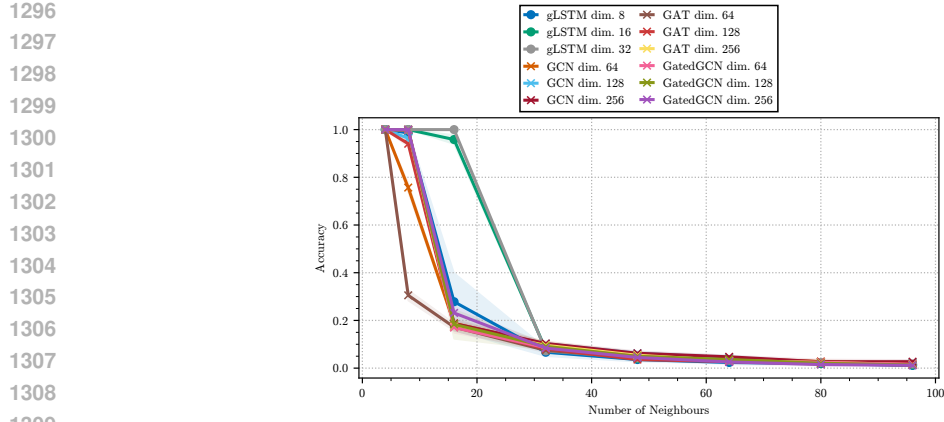


Figure 13: NAR Accuracy where all models do *not* use K-hop aggregation, for an expanded set of models.

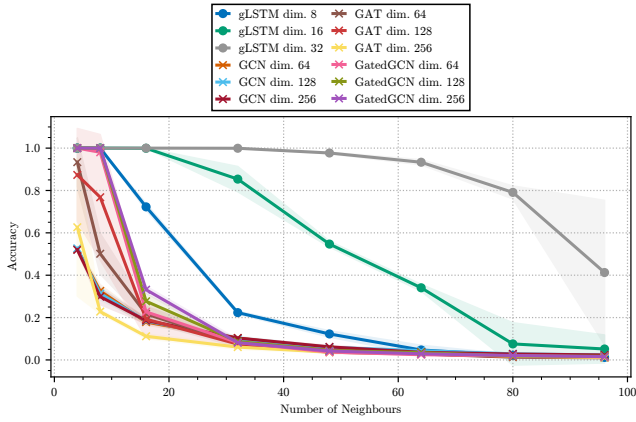


Figure 14: NAR Accuracy where all models *do* use K-hop aggregation, for an expanded set of models.

D.7.3 PERFORMANCE SEPARATED BY AGGREGATION STRATEGY

We next separate out no-K-hop and K-hop aggregation, and plot results for a larger set of models, in Figures 13 and 14 respectively.

We additionally verify that the number of layers is not the reason behind GCN being unable to solve NAR at higher neighbor counts. Figure 16 visualizes the performance of GCN models with hidden

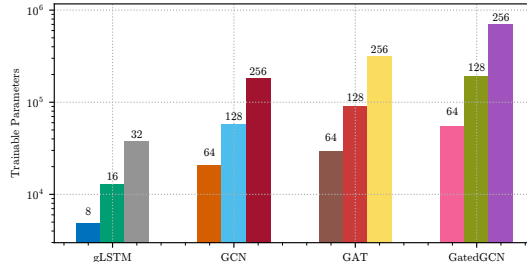


Figure 15: Number of trainable parameters for the expanded set of models tested in Figures 13 and 14.

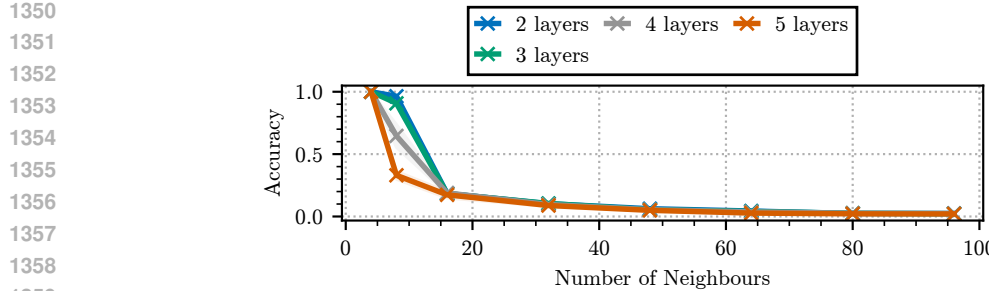


Figure 16: NAR Accuracy for GCN of hidden dimension 128, no K-hop, for varying numbers of GCN layers.

dimension 128 and various layer counts; it transpires that 2 layers performs best out of the tested layer counts.

D.7.4 ADDITIONAL SENSITIVITY METRIC RESULTS

We plot in this section the sensitivity metric trends of gLSTM vs GCN, both using K-hop aggregation.

Figure 17a visualizes the Jacobian norms for different model sizes and numbers of neighbors; Figure 17b shows the ratios between selected and background node Jacobian norms. Figure 18 separates out the Jacobian norms for gLSTM memory dimension 16 and GCN hidden dimension 64. Figure 19 visualizes the Hessian mixing metric for all models.

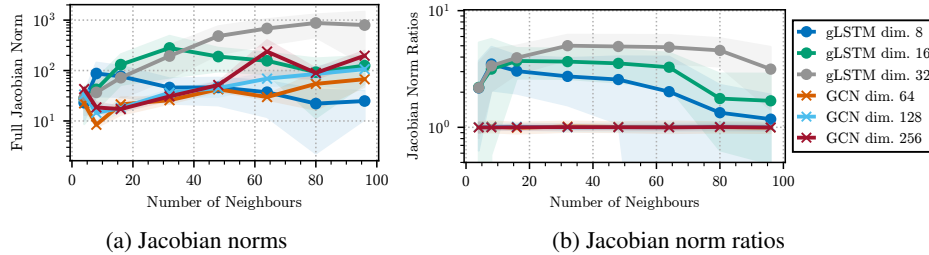


Figure 17: Left: Average Jacobian norms for different gLSTM and GCN models, with varying number of neighbors in the NAR task. Right: The ratio between the Jacobian norms of the selected (key corresponds to query) to background (key is different from query) neighbor nodes, for the different models - see Figure 18. This plot differs from that in the main body of the paper in that both gLSTM and GCN use K-hop aggregation.

D.8 NEIGHBOR ASSOCIATIVE RECALL REGRESSION RESULTS

In this section, we present results for the *regression* variant of the NAR task presented in the main body of the paper. We refer to this as Neighbor Associative Recall Regression (NARR).

Similarly to NAR, for a given neighborhood size N we create a graph of $N + 3$ nodes. This graph consists of N “neighbor” nodes, a central node to which they are all connected, and an intermediate node connected to the central node and a “query” node connected only to the intermediate node.

Each of the neighbor nodes has a feature vector representing a key and a value. The values consist of a fixed-dimensional vector of length V where each element is randomly sampled from a standard normal distribution. The keys are each unique one-hot vectors of dimension N . The query node’s feature vector contains a single one-hot vector, equal to one of the one-hot vectors of the neighbor nodes. The target of the graph is for the central node to predict the *value* of the neighbor node, corresponding to the key that matches the query node. Each node u is therefore equipped with an input feature vector $\mathbf{x} \in \mathbb{R}^{V+2N}$, where the first V elements comprise the value, the next N elements the key and the final N elements the query. Where a node does not have one of these features, the

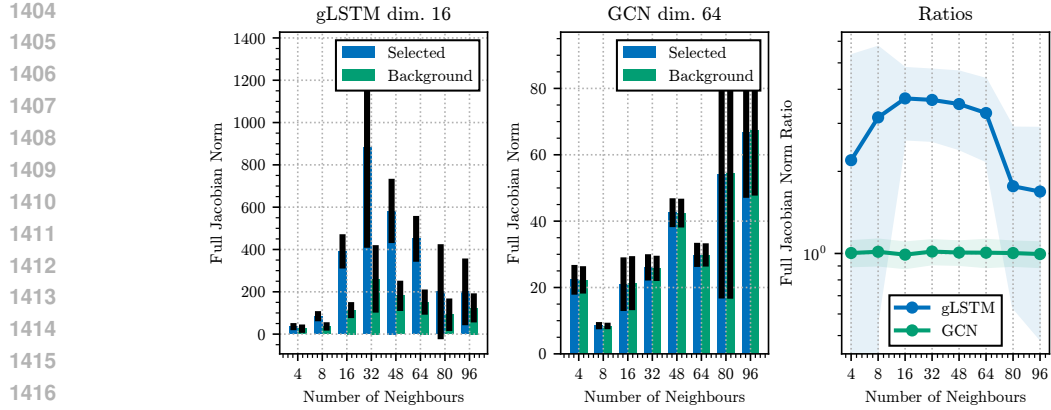


Figure 18: Left: Jacobian norms for gLSTM of memory dimension 16, with varying number of neighbors in the NAR task, separated by whether the neighbor node corresponds to the given query (selected) or not (background). Middle: Same, with GCN of hidden dimension 64. Right: Ratios of Jacobian norms for selected nodes to background nodes, for these two models. This plot differs from that in the main body of the paper in that both gLSTM and GCN use K-hop aggregation.

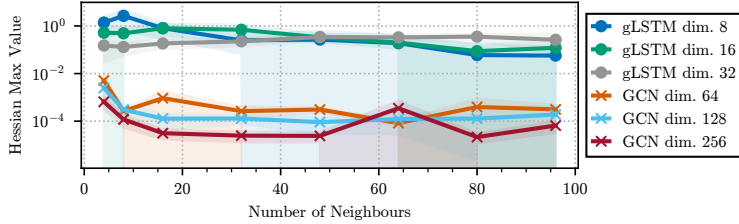


Figure 19: Mean of the maximum Hessian values for different gLSTM and GCN models, averaged across test set examples and different neighbor nodes. This plot differs from that in the main body of the paper in that both gLSTM and GCN use K-hop aggregation.

vector elements are set to zero. We note the use of one-hot encoding for keys and values means that the first linear layer of the model acts as a learned embedding function, where multiplication with the one-hot encoding simply selects the corresponding column of the weight matrix. For our experiments, we use $V = 16$.

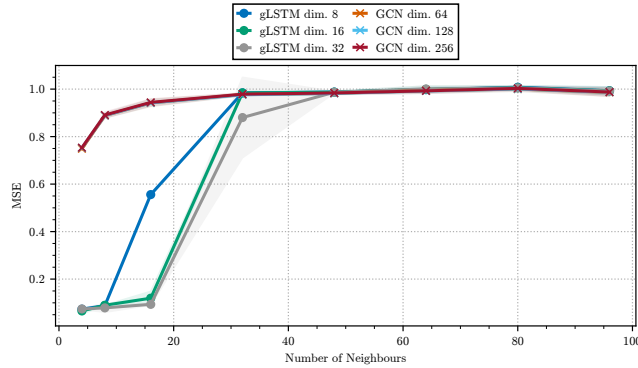
Since the value vectors lack the sparsity of NAR, this appears to be a “harder” task in the sense that it is more taxing on memory capacity. This means that some of the over-squashing trends are more defined, particularly trends in sensitivity-based measures - see Appendix D.8.1. However, our experiments suggest that the regression target means that NARR becomes too hard for vector-memory MPNNs to effectively solve, visible in Figures 20 and 21.

Performance (MSE) for NARR is shown in Figures 20 and 21 for no-K-hop and K-hop aggregation respectively. We note that the performance curves in Figure 21 look similar to those obtained by the sequence modeling variant of this experiment in Schlag et al. (2021). The number of trainable parameters is shown in Figure 22.

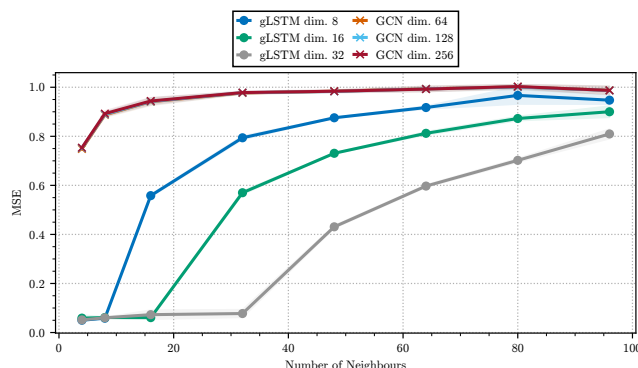
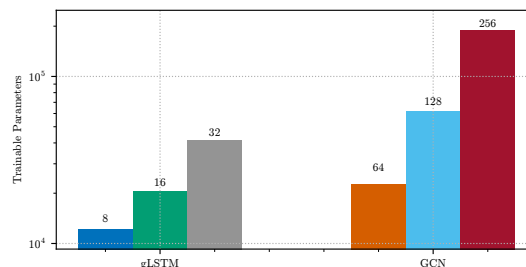
D.8.1 RELATIONSHIP TO OVER-SQUASHING SENSITIVITY METRICS

As with NAR in the main paper, we visualize the behavior of sensitivity-based over-squashing metrics for different neighbor counts and different models. Similarly to the main paper, we compare gLSTM using K-hop aggregation and GCN without. We note that – perhaps due to the increased difficulty of the task – the trends discussed in Section 5.2 are actually *more* pronounced for the NARR task.

Figure 23a visualizes the Jacobian norms for different model sizes and numbers of neighbors; Figure 23b shows the ratios between selected and background node Jacobian norms. Figure 24 separates

1458
1459
1460
1461
14621463
1464
1465
1466
1467
1468
1469
1470
1471
1472
1473
1474
1475
1476
1477
1478
1479
1480
1481
Figure 20: NARR MSE where all models do *not* use K-hop aggregation.

1470

1480
14811482
1483
1484
1485
1486
1487
1488
1489
1490
1491
1492
1493
1494
1495
1496
1497
1498
1499
1500
1501
1502
1503
1504
1505
1506
1507
1508
1509
1510
1511
Figure 21: NAR Accuracy where all models *do* use K-hop aggregation.1508
1509
1510
1511
Figure 22: Number of trainable parameters for the expanded set of models tested in Figures 20 and 21.

1512 out the Jacobian norms for gLSTM memory dimension 16 and GCN hidden dimension 64. Figure 25
 1513 visualizes the Hessian mixing metric for all models.
 1514

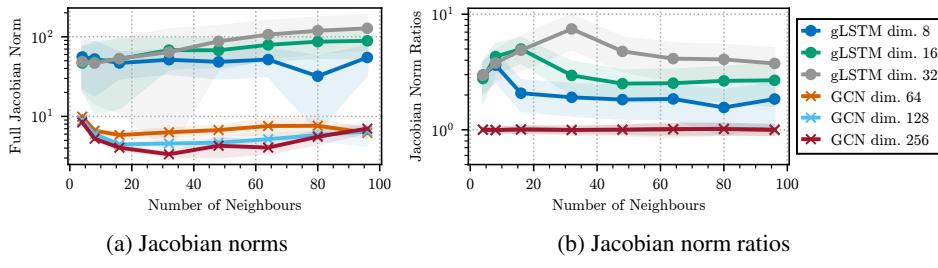


Figure 23: Left: Average Jacobian norms for different gLSTM and GCN models, with varying number of neighbors in the NARR task. Right: The ratio between the Jacobian norms of the selected (key corresponds to query) to background (key is different from query) neighbor nodes, for the different models - see Figure 24.

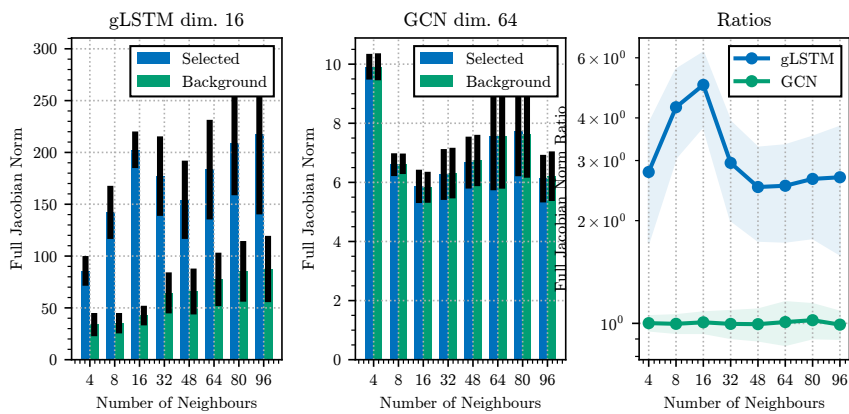


Figure 24: Left: Jacobian norms for gLSTM of memory dimension 16, with varying number of neighbors in the NARR task, separated by whether the neighbor node corresponds to the given query (selected) or not (background). Middle: Same, with GCN of hidden dimension 64. Right: Ratios of Jacobian norms for selected nodes to background nodes, for these two models.

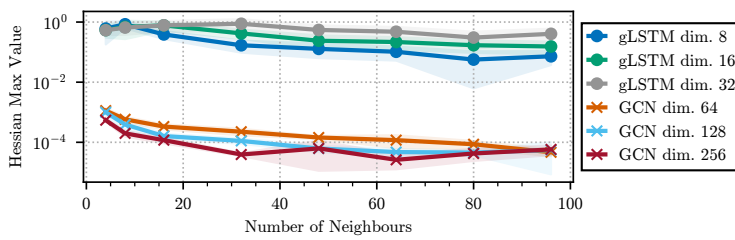


Figure 25: Mean of the maximum Hessian values for different gLSTM and GCN models, averaged across test set examples and different neighbor nodes.

We note that the sensitivity difference between selected and background nodes is particularly stark here, even more so for classification-based NAR; gLSTM consistently shows a sharp drop-off in Figure 23b at the memory dimension, and GCN maintains a ratio remarkably close to unity. This closely aligns with the performance of these models, Figure 21 demonstrates that gLSTM performance begins to drop off quickly when the number of neighbors matches the memory dimension, and Figure 20 demonstrates that GCN is never able to solve the task, for any tested number of neighbors.

We hypothesize that the strong impact of the K-hop aggregation on the model's ability to selectively recall - particularly visible for NARR - may partially explain the dramatic performance decrease

1566 when ablating this aggregation, discussed in Appendix D.2. We note that, while gLSTM con-
1567 sistently demonstrates superior performance to GCN, the improved performance is most striking when
1568 additionally using K-hop aggregation; it appears that the inductive bias introduced by the K-hop
1569 aggregation is particularly suited to the selective recall required by this task.
1570
1571
1572
1573
1574
1575
1576
1577
1578
1579
1580
1581
1582
1583
1584
1585
1586
1587
1588
1589
1590
1591
1592
1593
1594
1595
1596
1597
1598
1599
1600
1601
1602
1603
1604
1605
1606
1607
1608
1609
1610
1611
1612
1613
1614
1615
1616
1617
1618
1619